Metal-Insulator Transition and Orbital Ordering in $\mathbf{Y_{1-x}Ca_xTiO_3}$

Masami Tsubota

Department of Quantum Matter
Graduate School of Advanced Sciences of Matter
Hiroshima University

March, 2004

Abstract

Many of transition-metal oxides exhibit metal-insulator (MI) transitions induced by strong interactions between d-electrons. In the vicinity of the MI transition, various interesting phenomena, such as high-$T_{\rm C}$ superconductivity in cuprates and colossal magnetoresistance in manganites, have been discovered. To understand these phenomena, it is recognized that the orbital degree of freedom, in addition to the charge and spin degrees of freedom, should be taken into account. Recently, the role of orbital ordering in the dramatic change in transport and magnetic properties of manganites has been revealed by resonant x-ray scattering (RXS) techniques.

Among a large variety of transition-metal oxides, the perovskite-type titanium oxide, $YTiO_3$ and the Ca substituted alloys $Y_{1-x}Ca_xTiO_3$ have received much attention because of having smaller Jahn-Teller distortion relative to manganites. The parent material $YTiO_3$ is a Mott-Hubbard insulator in which one $3d$ electron of Ti^{3+} occupies the t_{2g} orbital keeping the e_g orbitals unoccupied. It is a rare example of having ferromagnetism below the Curie temperature $T_{\rm C} = 30$K. The origin of this ferromagnetic order has been considered to be a ferromagnetic superexchange interaction accompanied by antiferro orbital ordering of the t_{2g} orbitals. By the substitution of Ca^{2+} for Y^{3+} in $Y_{1-x}Ca_xTiO_3$, the ferromagnetic order disappears at $x_{\rm FP} \sim 0.2$, while the system remains insulating up to $x_{\rm MI} \sim 0.4$. For $x > x_{\rm MI}$, a metallic state becomes stable at room temperature. At the critical concentration $x = 0.39$, a first-order transition occurs from the insulating state to the metallic state upon decreasing temperature below about 150 K. The issues are not only the origin of the MI transition but also the reason why the value of $x_{\rm MI}$ is far above that of $x_{\rm FP}$. In analogy with the manganites, the orbital degree of freedom would play an important role in both the magnetic and metal-insulator transitions

To clarify these issues on $Y_{1-x}Ca_xTiO_3$, three approaches have been taken in the present study: (1) a comparison between the Ca substitution effect and pressure effect on the MI transition, (2) Rietveld analysis of the crystal structure by taking account of the $GdFeO_3$-type distortion (difference in bond angles of Ti-O-Ti) and the Jahn-Teller distortion (difference in Ti-O bond lengths), (3) study of orbital ordering by the techniques of RXS and polarized neutron diffraction (PND).

In Chapter 1, transport and magnetic properties of the $3d$ transition-metal oxides and Mott-Hubbard model for the MI transition are briefly described. The previous studies of $YTiO_3$ and $Y_{1-x}Ca_xTiO_3$ are also referred. Then, the purpose of the present study is presented.

Chapter 2 presents the methods of single-crystal growth of $Y_{1-x}Ca_xTiO_3$ and characterizations by x-ray diffraction analysis and electron-probe microanalysis.

Chapter 3 gives descriptions of experimental methods and techniques including the transport, magnetic and structural measurements. The PND, which provides the wave functions from the analysis of magnetic form factors, has been used to study orbital ordering in the ferromagnetic state for $x < 0.2$. The RXS technique, which is able to observe the orbital ordering from the analysis of the anisotropy of the atomic scattering factor, has been applied to study the substitution effect on the orbital ordering in the present system for $x \leq 0.75$.

In Chapters 4.1-4.3, the results of transport, magnetic, thermoelectric and structural measurements for $Y_{1-x}Ca_xTiO_3$ are presented and discussed, which are summarized as below.

(1) In Chapters 4.1 and 4.2, we made comparison between the Ca substitution effect and pressure effect on the transport and the structural properties. For several samples with $x \simeq x_{\rm MI}$, we measured the electrical resistivity $\rho(T)$ and powder x-ray diffraction (XRD) at ambient pressure. For $x = 0.37$ and 0.39, the MI transitions occur at $T_{\rm MI} = 100$ K and 150 K on cooling, respectively. Powder x-ray diffraction analysis showed that the monoclinic phase decomposes into a monoclinic phase and a low-temperature orthorhombic (LTO) phase on cooling below $T_{\rm MI}$. This LTO phase is found to be a metallic

phase from the fact that the residual resistivity decreases when the volume fraction of LTO increases. For $x = 0.37$, we measured $\rho(T)$ and XRD under pressure. The value of $T_{\rm MI}$ (100 K at $P = 0$ GPa) increases with increasing pressure, and eventually the metallic phase is stabilized even at room temperature under $P = 1.5$ GPa. The phase separation temperature agrees well with the $T_{\rm MI}$, and both temperatures increase linearly with increasing x or pressure. These results indicate that the MI transition in $Y_{1-x}Ca_xTiO_3$ is not a simple Mott-Hubbard type but is caused by the percolation of the metallic LTO domains.

(2) In Chapter 4.3, Rietveld analysis of room-temperature powder x-ray diffraction data is presented for the samples in the whole range $0 \leq x \leq 1$. It is found that the tilting angle of the TiO_6 octahedron (the Ti-O-Ti bond angle which is related to the magnitude of superexchange interaction) increases monotonously with increasing x from 0 to 1. On the other hand, the angle between the local coordination axes in the TiO_6 octahedron decreases from 93.5° for $x = 0$ to 92° for $x = 0.2$. Above $x = 0.2$, two Ti-O bond lengths in the *ab* plane become almost equal, *i.e.*, Jahn-Teller distortion is released. This structural change should be responsible for the disappearance of the ferromagnetism at $x = 0.2$.

In Chapters 4.4 and 4.5, the results of PND and RXS are presented and discussed, as summarized below.

(3) In the ferromagnetic region $x \leq 0.2$, we measured the magnetic form factors of Ti ions by means of PND in external fields parallel to the $c-$axis. The PND intensities have been observed at "*forbidden*" reflections in the conditions of $h + k = 2n + 1$, where h and k are the Miller indexes and n is an integer. By comparing the data with the model of orbital ordering configuration, we have determined the wave functions assuming $c_1|zx\rangle + c_2|xy\rangle$ ($c_1^2 + c_2^2 = 1$) at site 1, for example. The coefficient c_1 is determined to be 0.77 for $x = 0$ and $x = 0.05$. Above $x = 0.1$, however, c_1 could not be

determined uniquely. It is suggested that the ferromagnetic order becomes unstable when the order of orbitals is weakened.

The RXS experiments were performed for $0 < x \leq 0.75$ at room temperature. The main-edge RXS intensity at the $1s \rightarrow 4p$ transition energy of $E = 4.982$ keV decreases linearly with increasing x up to 0.2, and gradually decreases up to $x = 0.75$. On the other hand, the pre-edge intensity at the $1s \rightarrow 3d$ transition energy of $E = 4.972$ keV decreases rapidly with increasing x up to $x_{\rm FP}$ and vanishes at $x_{\rm MI}$. The x dependence of the RXS intensity at the main-edge has no dramatic change at both $x_{\rm FP}$ and $x_{\rm MI}$ and is unlike the x dependence of any local lattice distortion. The x dependence of RXS intensity at the pre-edge, on the other hand, is similar with that of Jahn-Teller (JT) distortion of the TiO_6 octahedron. This means that the RXS intensity at the pre-edge reflects the orbitally ordered state. Thus, we have found that the ordering is weakened above $x = x_{\rm FP}$ but remains in the whole insulating phase for $x < x_{\rm MI}$.

By combining the above results (1), (2), and (3), it is found that the temperature-induced MI transition in $Y_{1-x}Ca_xTiO_3$ at $x \sim 0.39$ is not a simple Mott-Hubbard type but is a result of percolation of domains of the metallic low-temperature orthorhombic phase. For the insulating phase for $0 < x < 0.2$, the strong evidence of orbital ordering is obtained by both polarized neutron diffraction and resonant x-ray scattering experiments. It is concluded that the magnetic order becomes unstable when the order of orbitals is weakened, and the metallic phase appears when the order of orbitals melts for $x > 0.4$ in $Y_{1-x}Ca_xTiO_3$.

Contents

List of Figures

List of Tables

Chapter 1

Introduction

Metal-insulator (MI) transitions are widely observed in condensed-matter systems, which are accompanied by huge resistivity changes, even over tens of orders of magnitude. The MI transitions in transition-metal oxides are often driven by strong interactions between d-electrons. This chapter describes basic properties of transition-metal oxides and the previous studies of $YTiO_3$, $Y_{1-x}Ca_xTiO_3$ and related compounds.

1.1 Mott-insulators and orbital ordering

1.1.1 Mott insulators in 3d transition-metal oxides

In the field of transition-metal oxides, the so-called Mott insulator, that is an insulating state induced by a transition from a metalic state, has been extensively investigated [1–6]. The Mott insulator is a model, which was proposed by Mott in 1949, to understand the MI transitions due to the strong correlation between d-electrons. Mott considered a lattice model with a single electronic orbital on each site. Without electron-electron interactions, a single band would be formed by the overlap of atomic orbitals, where the band becomes full when two electrons, one with up-spin and the other with down-spin, occupy each site. However, two electrons sitting on the same site would feel a large Coulomb repulsion, which split the band into two. The lower band in energy is formed by electrons that singly occupies one site and the upper one by electrons that occupy a site already occupied by

another electron, respectively. The lower band filled by one electron per site should make the system an insulator. In the Mott insulators, the MI transition from an insulator to a metal takes place with decreasing U or with increasing t. Here, U is the intra-atomic Coulomb energy of a d-electron orbital and t is a transfer integral between the unoccupied d-band and the filled p-band of ligand oxygens neighboring d-atoms [2]. To understand the electron correlation effects in the MI transition, the Mott-Hubbard model with the parameter of the ratio U/t is often used. In the case $U \gg t$, the system is insulating due to the strong repulsion between electrons, whereas in the case $U \ll t$, the system becomes metallic.

Zaanen, Sawatzky and Allen (ZSA) have pointed out that the insulator of $3d$ electron systems can be classified into two categories as shown in Fig 1.1 [7]. One is the Mott insulator (so-called Mott-Hubbard (MH) insulator), where the charge gap is governed by the Hubbard splitting (U) of the d-band. The other is the so-called charge transfer (CT) insulator, where the charge gap is typically an energy difference (Δ) between filled p-bands of ligand anions and the unoccupied upper Hubbard $3d$ band. In general, t_{2g}-electrons system such as titanates and vanadetes, in which t_{2g} orbitals are partially filled and e_g orbitals are unoccupied, are classified to the MH-type insulator. On the other hand, e_g-electrons system such as manganites and cuprates, in which t_{2g} orbitals are fully occupied and e_g orbitals are partially filled, are the CT-type insulator.

Near the MI transition point, the physical properties at these metallic region are frequently quite different from those of ordinary metals, as measured by transport, magnetic and optical probes. Various interesting phenomena, such as high-T_c superconductivity in cuprates and colossal magnetoresistance in manganites, have been discovered in the vicinity of the MI transition. Although electron-electron interactions indeed play the central role in these phenomena, we should take account of another aspect of electrons — orbital degrees of freedom.

1.1.2 Orbital Ordering

Here, we focus on a perovskite-type manganese oxide $Nd_{1/2}Sr_{1/2}MnO_3$. This material is one of the typical charge-ordering oxides showing a colossal negative magnetoresistance

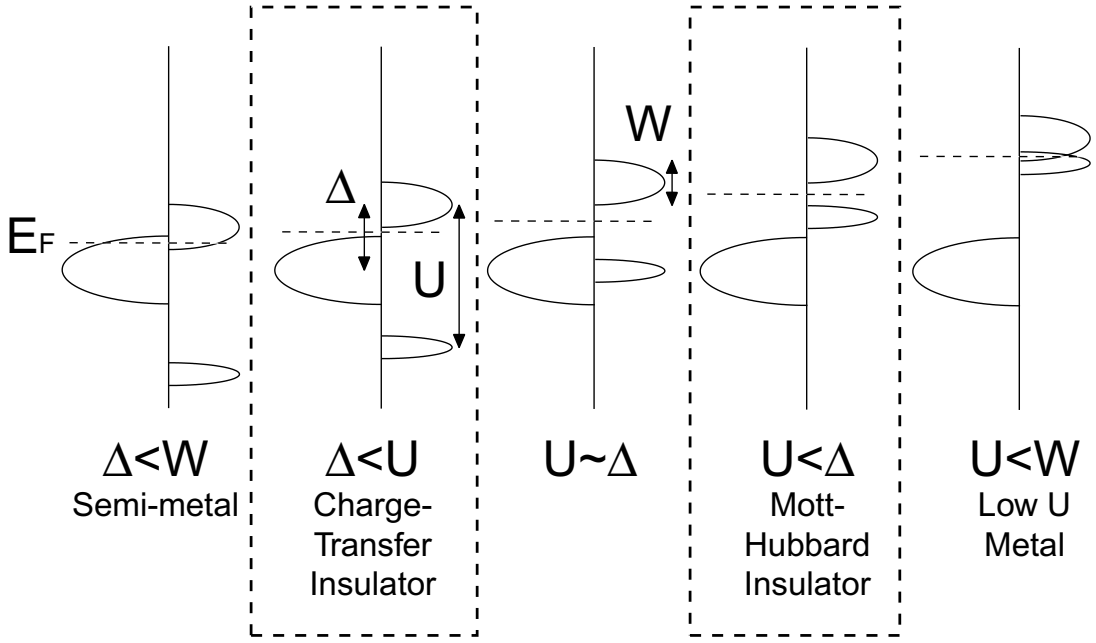

Figure 1.1: Zaanen-Sawatzky-Allen Framework [7].

(CMR) [9]. At room temperature it is a paramagnetic metal and shows ferromagnetism below the Curie temperature $T_{\rm C} = 255$ K. On further cooling, a first-order metal-to-insulator transition is observed at the charge-ordering temperature $T_{\rm CO} = 150$ K as shown in Fig. 1.2. To understand the mechanism of this jump at $T_{\rm CO}$ K in the electrical resistivity, the possibile charge ordering (CO) was investigated by various methods. In fact, superlattice reflections were observed at $Q_{\rm charge} = (0, 1, 0)$ in the $Pbnm$ symmetry by a resonant x-ray scattering method [27]. This observation of superlattice reflections was the discovery of the charge ordering in this manganese oxide. To date, it has been found that many transition-metal oxides such as $LaMnO_3$, $La_{1.5}Sr_{0.5}MnO_4$ show charge and/or orbital ordering [18, 24].

Now, it is well recognized that the orbital degree of freedom, in addition to the charge and spin degrees of freedom, plays an important role in determining the electronic and magnetic properties of transition-metal oxides. Among perovskite-type $3d$ transition-metal oxides, the e_g-electron system such as manganites, exhibits a large Jahn-Teller distortion in the MnO_6 octahedron due to a strong electron-lattice coupling. The resultant orbital ordering has attracted much attention [18]. Despite the electron-lattice coupling

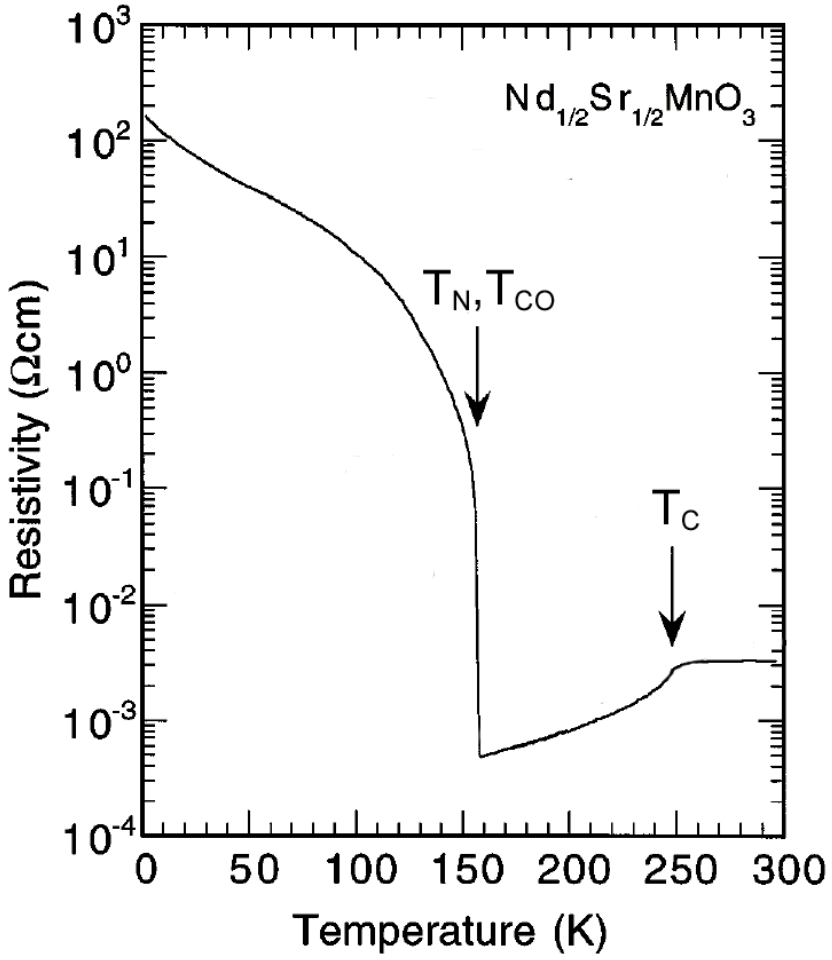

Figure 1.2: Temperature dependence of the electrical resistivity of $Nd_{1/2}Sr_{1/2}MnO_3$. Arrows denote transition temperatures, T_C; the Curie temperature, T_{CO}; the charge-ordering temperature and T_N; the Néel temperature [9].

in the t_{2g}-electron system is weaker than that in the e_g-electron system, orbital ordering occurs in certain t_{2g}-electron systems like YVO_3 and $YTiO_3$ [8, 13, 15, 19, 21]. $YTiO_3$ is considered as a typical Mott-Hubbard insulator. In this thesis, we focus on $YTiO_3$ and $Y_{1-x}Ca_xTiO_3$.

1.2 Physical properties of $YTiO_3$ and $Y_{1-x}Ca_xTiO_3$

$YTiO_3$ is a d^1-system, which is well known as a Mott-Hubbard insulator with a value of $U \sim 1$eV [3]. The ferromagnetic state [35–38] with a Curie temperature $T_C \sim 30$ K is atypical for a Mott insulator because most of Mott insulators are antiferromagnetic as seen in $LaTiO_3$ and V_2O_3 [5, 6]. $YTiO_3$ crystallizes in an orthorhombic perovskite (so-called $GdFeO_3$-type) structure as shown in Fig. 1.3. The $GdFeO_3$-type perovskite is a distorted derivative of a cubic perovskite (see Fig. 1.5). The axes of TiO_6 octahedra in a $GdFeO_3$-type structure tilt from the principal crystal axes. The distorted bond angle of Ti-O-Ti is approximately 140° [17]. $YTiO_3$ also shows a Jahn-Teller distortion of the type d as shown in Fig. 1.4, where the longer and shorter Ti-O bonds are ~ 2.08 Å and ~ 2.02 Å, respectively [17].

In Ca substituted alloys $Y_{1-x}Ca_xTiO_3$, the number of $3d$ electrons per Ti atom can be controlled from 1 to 0 with increasing Ca content x from 0 to 1, and thereby hole carriers are doped at the Ti site. The previous studies on $Y_{1-x}Ca_xTiO_3$ by using polycrystalline samples revealed that the ferromagnetism vanishes at $x \sim 0.15$, while the system remains insulating up to $x \sim 0.4$ [3, 4, 39–44]. Above $x \sim 0.4$, the system changes into a metallic state below room temperatures. For $x = 0.37 \sim 0.39$, a temperature induced transition from the insulating state to the metallic one occurs upon decreasing temperature [3,4,39–43]. At the critical concentration $x_{cr} = 0.39$, the electrical resistivity $\rho(T)$ drops by two orders of magnitude at 150 K [3,4,40–43]. Upon approaching x_{cr} from the metallic region, both the electronic specific-heat coefficient and Pauli's paramagnetic susceptibility are significantly enhanced [4, 39]. This enhancement was taken as an experimental evidence for the divergence in the carrier mass. Thus, the MI transition in $Y_{1-x}Ca_xTiO_3$ had been considered as a typical example of a Mott-Hubbard type transition [2].

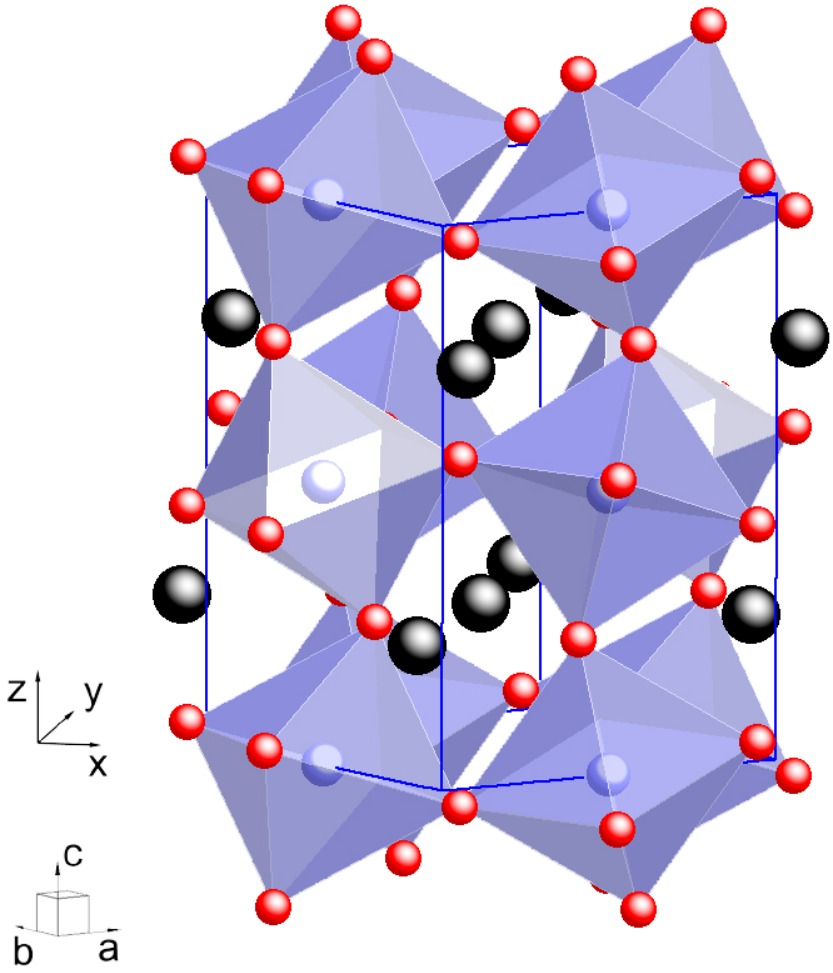

Figure 1.3: The crystal structure of the $GdFeO_3$-type perovskite. In the case of $YTiO_3$, it shows a Jahn-Teller distortion of type *d*, in which the elongated TiO_6 octahedron are alternatively arranged in the *ab*-plane. The same pattern repeats along the *c*-axis [17].

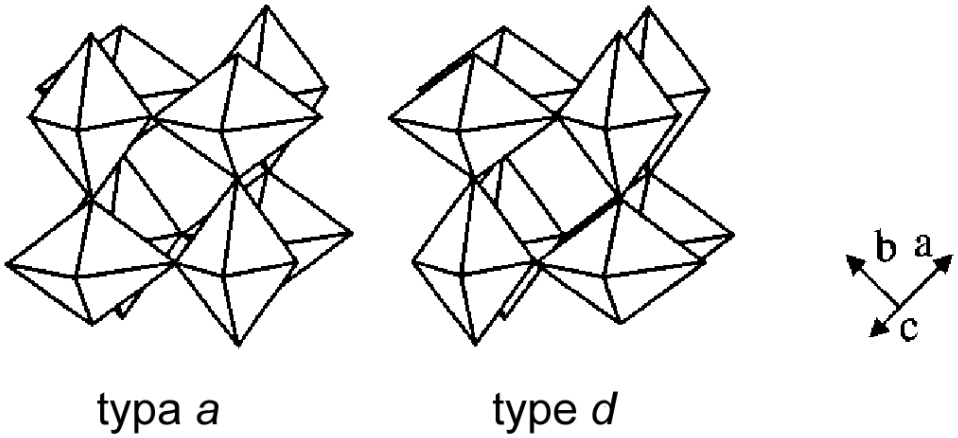

Figure 1.4: Two types of Jahn-Teller distortion. In the case of $YTiO_3$, it shows a Jahn-Teller distortion of type d, [17].

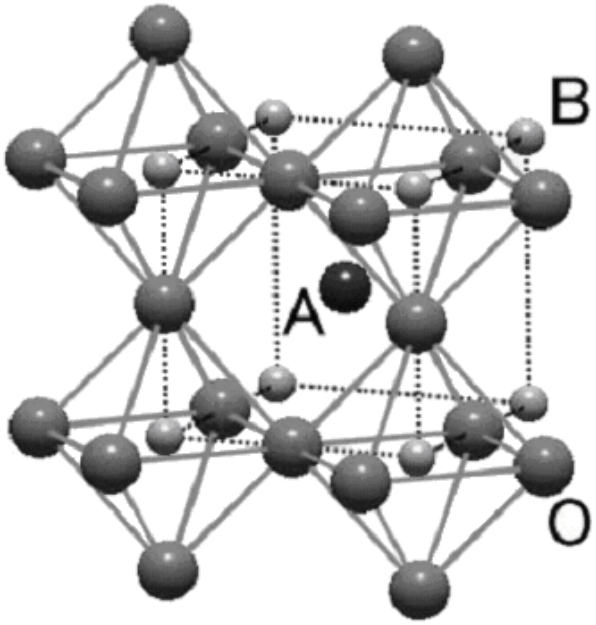

Figure 1.5: The crystal structure of the cubic perovskite.

More recently, temperature-dependent structural transformations have been found in the vicinity of the MI transition [45]. The high-resolution powder x-ray diffraction experiments on samples for $x = 0.37$ and 0.39 have revealed a phase transition from orthorhombic (space group $Pbnm$) to monoclinic ($P2_1/n$) occurring at $T \sim 230$ K on cooling. For the monoclinic phase, the angle β between the a and c axes gradually increases from 90° up to 90.15°. On further cooling below 100 K and 150 K for $x = 0.37$ and 0.39, respectively, a low-temperature orthorhombic phase (LTO, space group $Pbnm$) appears and coexists with the monoclinic phase. For $x = 0.41$, the two phases coexists even at room temperature. The volume fraction of the LTO phase increases with decreasing temperature and saturates to the value of 25, 80 and 90% for $x = 0.37$, 0.39 and 0.41, respectively, at 10 K. Since the MI transition associated with such a phase separation is beyond the conventional theory based on the Mott-Hubbard model, further studies on the MI transition of $Y_{1-x}Ca_xTiO_3$ are necessary.

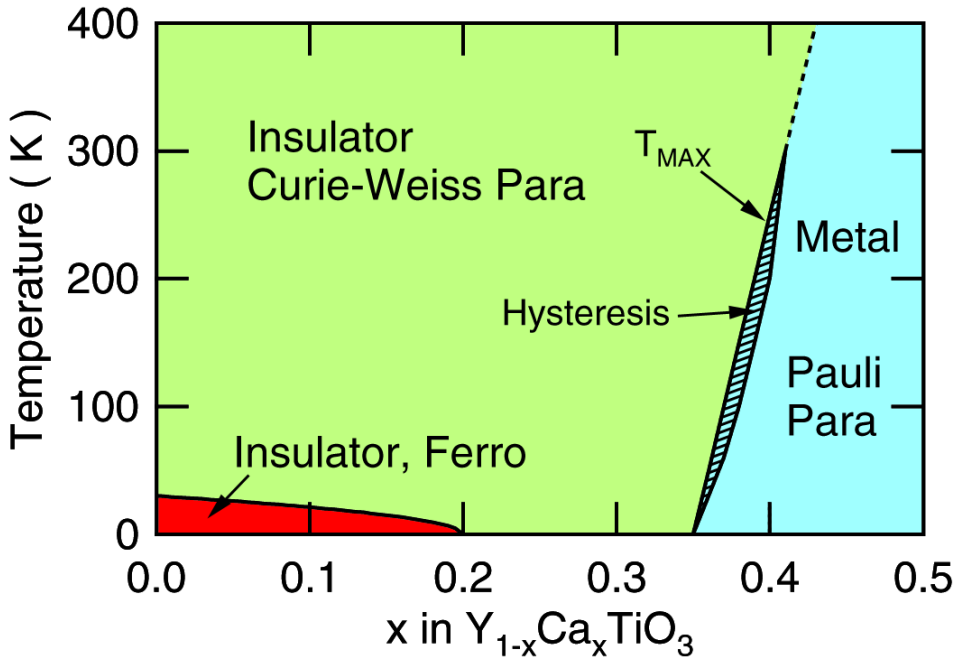

Figure 1.6: The $x - T$ phase diagram of $Y_{1-x}Ca_xTiO_3$.

1.3 Purposes of the present study

In this thesis, we focus on the t_{2g}-electron system of titanate $YTiO_3$ and its Ca subsutituted compounds $Y_{1-x}Ca_xTiO_3$. To clarify the role of the orbital degree of freedom both in the magnetic transition and the metal-insulator one in $Y_{1-x}Ca_xTiO_3$, three approaches have been taken in the present study: (1) a comparison between the Ca substitution effect and pressure effect on the MI transition, (2) Rietveld analysis of the crystal structure to estimate the $GdFeO_3$-type tilting distortion (difference in bond angles in Ti-O-Ti) and the Jahn-Teller distortion (difference in Ti-O bond lengths), (3) observation of orbital ordering by polarized neutron diffraction (PND) and resonant x-ray scattering (RXS) techniques.

Chapter 2

Crystal growth and characterizations of $Y_{1-x}Ca_xTiO_3$

2.1 Single-crystal growth

For the single-crystal growth of $Y_{1-x}Ca_xTiO_3$ $(0 \leq x \leq 1)$, we used $CaCO_3$, TiO_2, Ti_2O_3 and Y_2O_3 with purity of 4N, 3N, 3N and 4N as starting materials, respectively. Single crystals were prepared by the following sequence. At the first step, the mixture of $CaCO_3$ and TiO_2 was heated in an alumina crucible in air at 1000 °C for 36 hours by using a resistive heating furnace (muffle furnace). Thereby, the following reaction occurs,

$CaCO_3 + TiO_2 \rightarrow CaTiO_3 + CO_2 \uparrow$.

Thus obtained polycrystalline sample $CaTiO_3$ was mixed with powders of Y_2O_3 and Ti_2O_3, and the mixture was stuffed into a rubber tube. The mixed powder was isostatically pressed up to 180 kgf/cm^2 into a rod of 8 mm in diam. and 100 mm in length. The rod was inserted into a boron nitride tube and heated in a vacuum at about 1000 °C for 45 minutes by a high-frequency induction heating furnace (see Fig. 2.1).

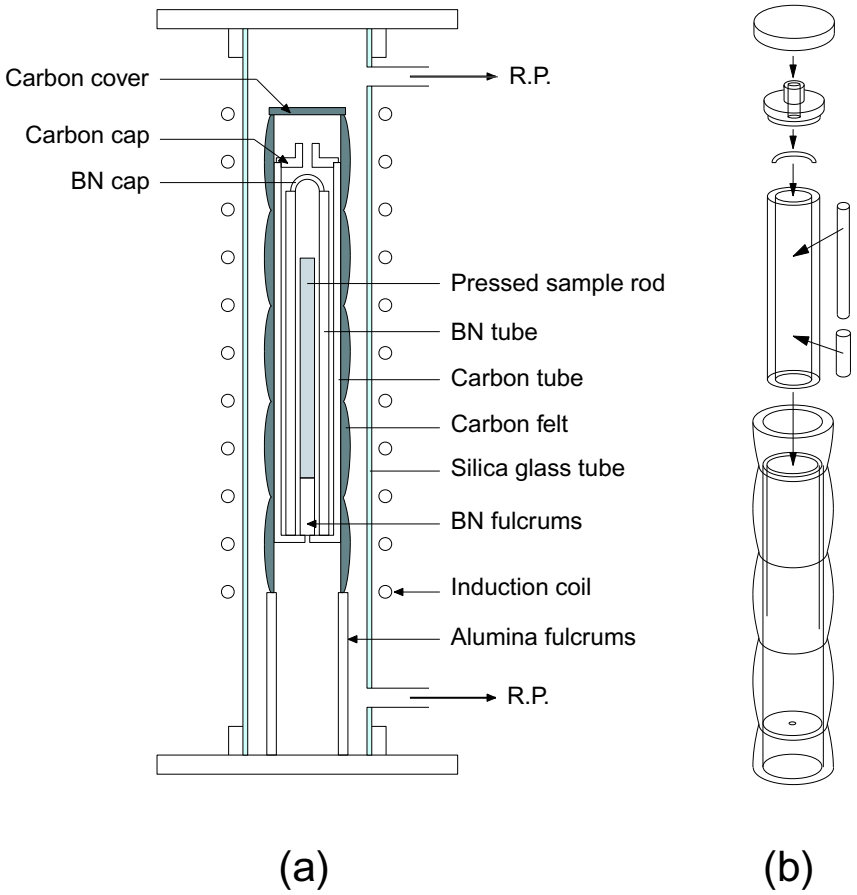

Figure 2.1: Schematic diagram of the high-frequency induction heating furnace used for sintering; (a) overview of the furnace and the carbon tube with the sample rod, (b) details of assemblies for setting the sample rod in the BN tube.

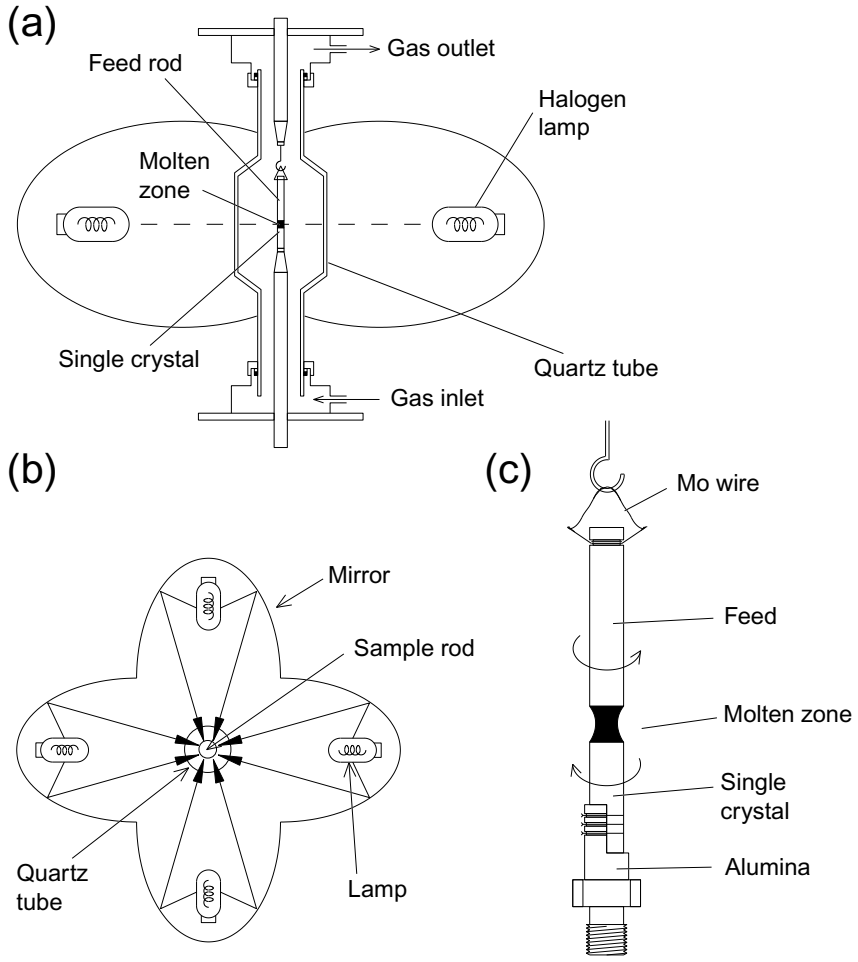

Figure 2.2: Schematic diagram of the ellipsoidal mirror furnace equipped with four halogen lamps. This furnace was used for the crystal growth by the floating zone method; (a) side view, (b) top view and (c) enlarged view of sample.

Thereby the following reaction takes place,

$(1-x)\ (Y_2O_3 + Ti_2O_3) + x\ CaTiO_3 \rightarrow Y_{1-x}Ca_xTiO_{3-y} + \frac{y}{2}O_2 \uparrow$.

Here, it is noted that powder x-ray diffraction analysis of the sintered rod showed the presence of a few % of raw materials of Y_2O_3 and Ti_2O_3 and oxidized $Y_2Ti_2O_7$ with the pyrochlore structure. The rods were used to grow single crystals by a floating zone method being free from contamination from a crucible (see Fig. 2.2).

Figure 2.3: Photograph of the as-grown single crystal of $YTiO_3$.

The feed rod was hung by Mo wires at the center of an ellipsoidal mirror furnace equipped with four halogen lamps. A molten zone was scanned by a speed of 10 mm/h in a reduction atmosphere of mixture of Ar 50% and H_2 50% at the flow rate of 5 ℓ/min. The typical size of a single crystal was of 8 mm in diam. and 80 mm in length as shown in Fig. 2.3.

Thermogravimetric analysis (TGA) of the as-grown crystal indicated the oxygen deficiency y in $Y_{1-x}Ca_xTiO_{3-y}$ to be $0.02 - 0.05$. Therefore, the crystal was heat-treated in air at 400 °C for 4 hours to recover the oxygen stoichiometry. This heat-treating condition was determined by TGA measurements at different temperatures and periods.

2.2 Characterization of samples by x-ray diffraction analysis and electron-probe microanalysis

The single-crystal nature of the $Y_{1-x}Ca_xTiO_3$ sample was examined by Laue photos, powder x-ray diffraction analysis and electron-probe microanalysis (EPMA). The Laue pattern indicated that the crystal structure is of the orthorhombic $GdFeO_3$-type with the space group of *Pbnm* at room temperature. Powder x-ray diffraction showed that all the samples for $0 \leq x \leq 1$ are the single phase. The x-ray diffraction patterns and estimated lattice parameters are listed in Fig. 2.4 and Table. 2.1, respectively. EPMA showed that there is no deviation of the Ca concentration from the nominal value within the accuracy of 1% for the whole rod.

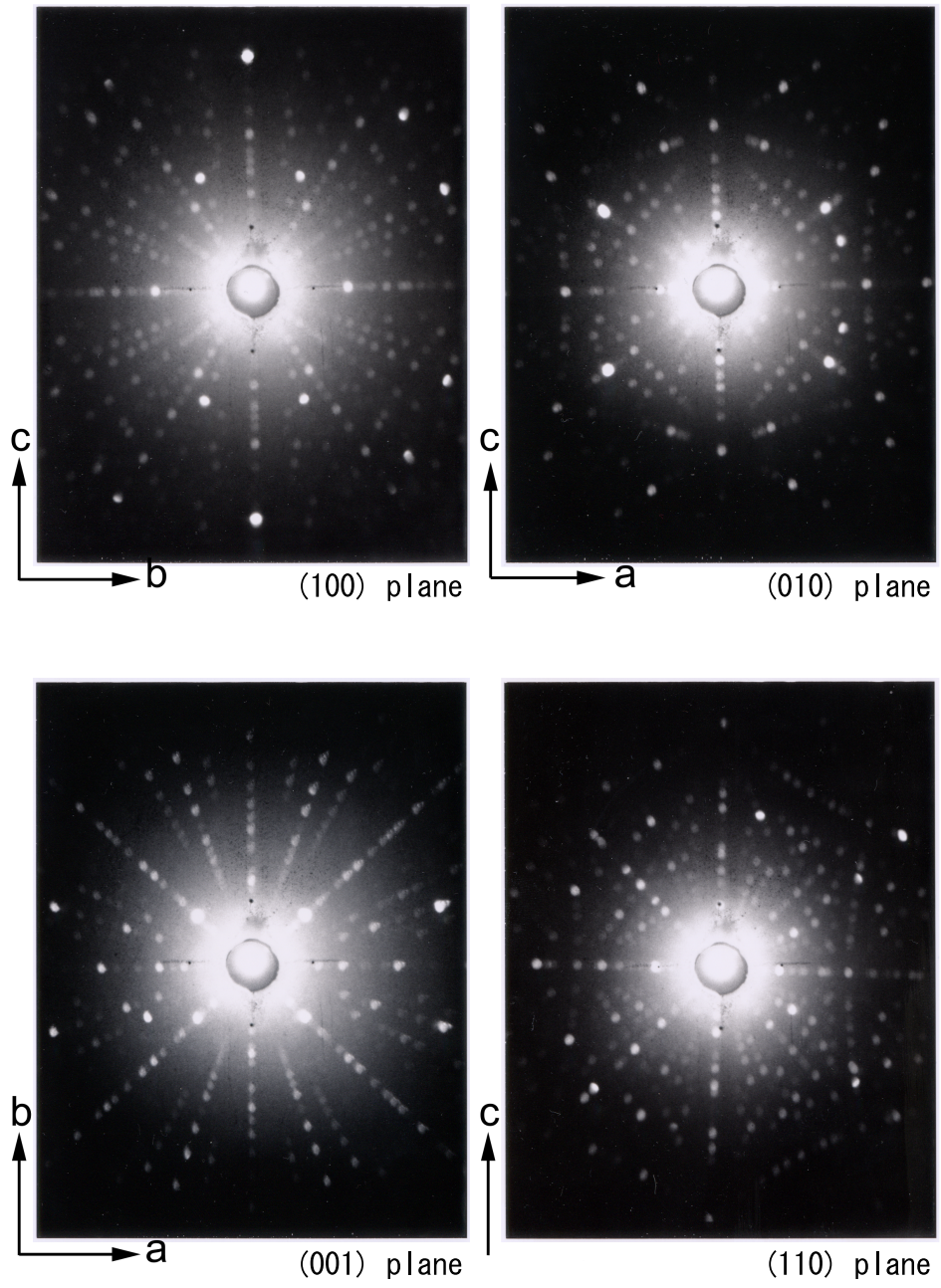

Figure 2.4: Laue photos of the single crystal of $YTiO_3$.

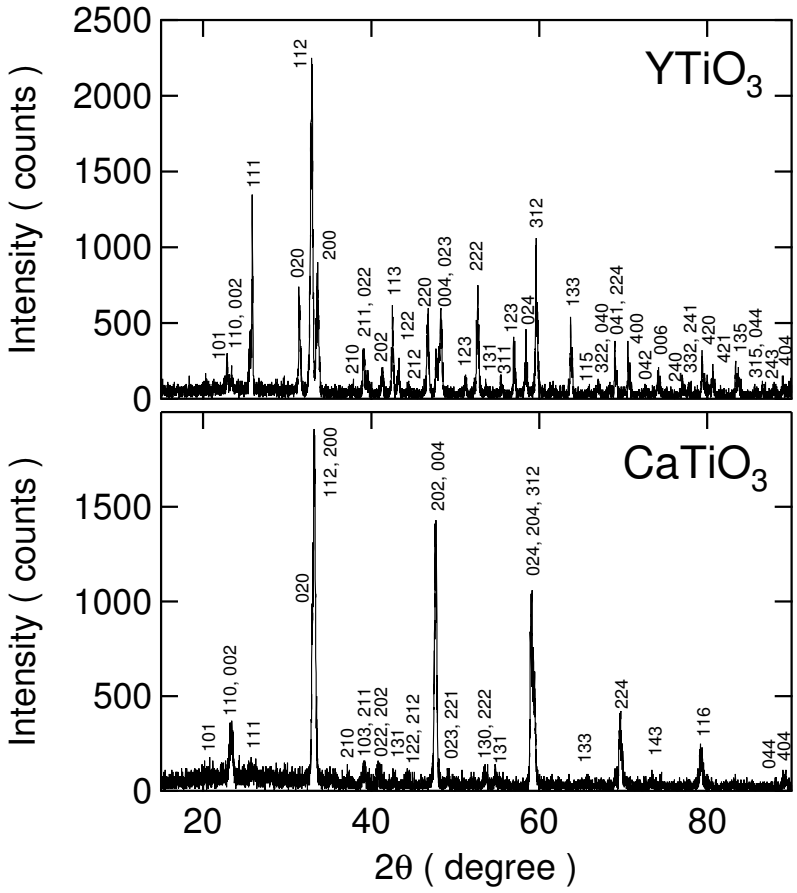

Figure 2.5: Powder x-ray diffraction patterns of $YTiO_3$ and $CaTiO_3$ taken by using Cu Kα radiation.

Table 2.1: Lattice parameters of $YTiO_3$ and $CaTiO_3$ with the orthorhombic $GdFeO_3$-type structure.

Compounds	Lattice parameters		
	a (Å)	b (Å)	c (Å)
$YTiO_3$	5.338	5.683	7.615
$CaTiO_3$	5.381	5.445	7.648

Chapter 3

Experimental methods

3.1 Electrical resistivity

The electrical resistivity was measured from 1.3 to 300 K by a conventional four-probe method. Four leads of gold wires (ϕ 50 μm) were fixed on the sample by silver paste. The contact resistance between the wire and the sample was a few 10 Ω. The electrical resistivity under quasi-hydrostatic pressure was measured in the temperature range from 1.3 to 300 K. Hydrostatic pressure up to 2 GPa was applied by using a clamp-type piston-cylinder pressure cell. This cell is made of hardened beryllium-copper. Daphne oil was used as the pressure transmitting medium. Pressure was determined from the known pressure dependence of the electrical resistance of a manganin wire.

3.2 Magnetic susceptibility and magnetization

The magnetic susceptibility and magnetization were measured by using a commercial superconducting quantum interface device (SQUID) magnetometer (MPMS, Quantum Design). The magnetic susceptibility was measured in the temperature range from 2 to 350 K in fields of 1, 10, 100 mT and 1 T. The measurements of magnetization were performed in fields from 0 up to 5 T at 2 K for ferromagnetic samples.

3.3 Powder x-ray diffraction

High resolution powder x-ray diffraction (XRD) experiments for detailed analysis of crystal structure were performed by using synchrotron radiation at SPring-8 and Photon Factory. The powdered samples were prepared by crushing the high-quality single crystals. The powder size was made less than 3 μm by a precipitation method in order to obtain a homogeneous intensitiy distribution in the Debye-Scherrer powder ring. In the precipitation method, we followed a following procedure.

1. The single crystals are crushed into powder with a pestle and a mortar made of agate for 1 hour.

2. The powder is precipitated in methanol for 1 hour.

3. Supernatant liquid is skimmed and dried well.

The obtained powder sample was sealed in the soda glass capillary tube of 0.2 mm in diam. For the samples of $Y_{1-x}Ca_xTiO_3$ with $x = 0.37, 0.39$ and 0.41, XRD measurements at various temperature from 20 K to 300 K were carried out by a large Debye-Scherrer camera installed at the beam line BL-02B2, SPring-8 [10]. A He-gas circulation-type cryostat was used for the temperature variation from 300 K down to 20 K at intervals of 20 K. The data were collected by a 0.01° step from 8.0° to 74.0° in 2θ for the x-ray exposure time of 32 min.

The powder x-ray diffraction for $0 \leq x \leq 1$ was measured at room temperature by the micropowder diffractometer at the BL-1B, Photon Factory, KEK [11]. The x-ray exposure time was 10 to 60 min, depending on the filling factor and the intensity of the incident radiation. The XRD pattern was recorded by a 0.04° step from -44.0° to 122.0°.

Powder x-ray diffraction experiments under pressure up to 2 GPa were carried out at BL10XU, SPring-8 by using a diamond anvil cell (DAC). Pressure was generated in the DAC through a 1:1 mixture of methanol/ethanol as pressure transmitting medium. On both cooling and heating, the pressure was kept constant by the adjustment of the gas pressure loaded to the membrane which holds the gasket in the DAC. The absolute value of loaded pressure was determined from the pressure dependence of the wavelength in the

fluorescence line of a ruby chip enclosed in the DAC. Temperature dependences of the XRD patterns were obtained from 10 K up to 230 K for the sample of $x = 0.37$.

The wavelength of the incident x-ray was selected to be 0.735 Å ($E \sim 16.9$ keV) to avoid the large background due to the K-edge scattering (0.728 Å; $E \sim 17.0$ keV) from yttrium atoms in the sample. The structural parameters ($a, b, c, \alpha, \beta, \gamma$, atomic positions) were determined by the Rietveld analysis with the RIETAN-2000 program [12]. In the analysis, the set of parameters $\boldsymbol{x}$ was determined to minimize the following described $S(\boldsymbol{x})$ by a nonlinear least-squares method,

$$S(\boldsymbol{x}) \;\; = \;\; \sum_i w_i [y_i - f_i(\boldsymbol{x})]^2,$$

where y_i, $f_i(\boldsymbol{x})$ and $w_i (= 1/y_i)$ are the measured intensisy at the diffraction angle $2\theta_i$, a calculated intensity and statistical weight of the data, respectively.

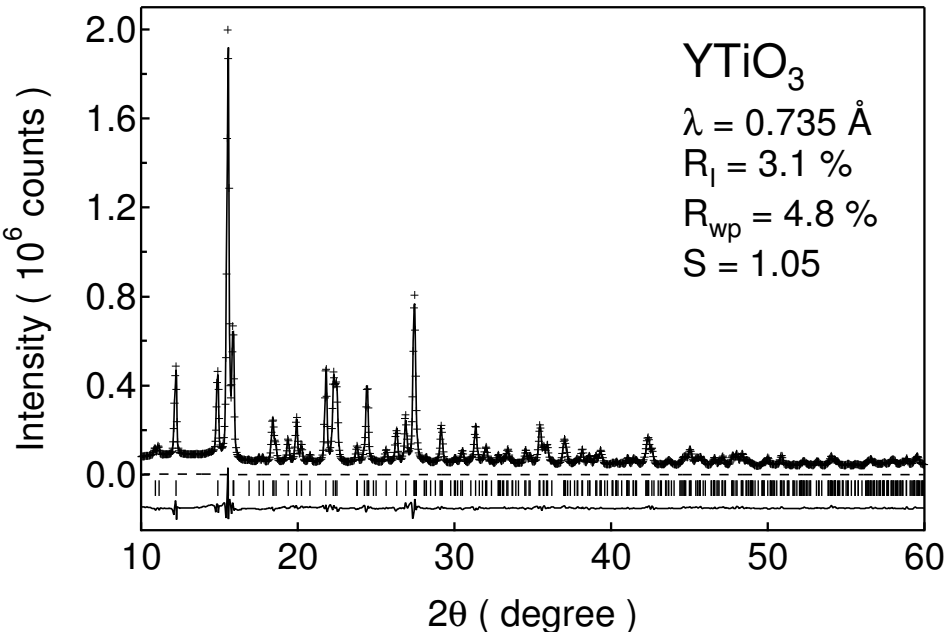

Figure 3.1: Rietveld fitting of the x-ray diffraction pattern of $YTiO_3$ measured at the BL-1B, PF, KEK.

3.4 Polarized neutron diffraction

Polarized neutron diffraction (PND) technique is a powerful method to observe the orbital ordering in a ferromagnet [14]. The advantage of this technique is that it can directly determine the accurate wave functions for the orbital ordered state. The disadvantage is that it is useful only below the Curie temperature $T_{\rm C}$. To determine the wave function, we compare the magnetic form factor $\mu f(\boldsymbol{K})$ experimentally observed with that calculated for some supposed wave functions, where $\boldsymbol{K}$ is the scattering vector.

For the PND measurements, we measured the forbidden magnetic diffractions which satisfy the conditions of $h + k = 2n + 1$, where h and k are the Miller indices and n is the integer. This means that these *special* magnetic diffractions should appear with the existence of the antiferro orbital ordered configuration. These diffractions originate from the aspherical contribution of the spin density distribution.

In order to obtain the magnetic form factor, we measured some pairs of the reflection for both parallel spin (spin flipper off) and anti-parallel (on) to the direction of applied magnetic field B which saturates the magnetization as shown in Fig 3.2. From the observed reflection intensities $C_{\rm off}$ and $C_{\rm on}$ for each reflection lines at the flipper off and on, we obtain the ideal intensities of I_+ and I_-, where the subscripts "off" and "on" stand for the switching arrangement of a spin flipper equipment, and + and − denote that the neutron spin is parallel and anti-parallel for the direction of B, respectively. Here, I_+ and I_- is derived from C, the monitoring time M, the background intensities BG and poralization ratio of a spin flipper p as following;

$$I_+ = \frac{pI_{\rm off} - (1-p)I_{\rm on}}{2p-1} \quad , \quad I_- = \frac{pI_{\rm on} - (1-p)I_{\rm off}}{2p-1} \ ,$$

where $I_{\rm on}$ and $I_{\rm off}$ is a normalized intensity when the flipper on and off, respectively,

$$I_{\rm on} = \frac{C_{\rm on}}{M_{\rm on}} - \frac{BG_{\rm on}}{M_{\rm BG}} \quad , \quad I_{\rm off} = \frac{C_{\rm off}}{M_{\rm off}} - \frac{BG_{\rm off}}{M_{\rm BG}} \ .$$

In the analysis of PND, the observed polarization ratio R, which is the ratio of the intensities I_+ and I_-, was related to $\gamma_0 = F_M/F_N$ after instrumental corrections as below,

$$R \ = \ \frac{I_+}{I_-} = \left(\frac{F_N + F_M}{F_N - F_M}\right)^2 = \left(\frac{1+\gamma_0}{1-\gamma_0}\right)^2 ,$$

where F_M and F_N are the magnetic structure factor and the nuclear structure factor, respectively. Here, we used the knowledge of F_N which was obtained from the Rietveld analysis of powder x-ray diffraction data for each sample of $Y_{1-x}Ca_xTiO_3$ ($x = 0.05, 0.10$ and 0.15). The magnetic form factor μf is expressed as following;

$$\mu f(\boldsymbol{K}) = \frac{2F_M}{\sum_j D \exp\{2\pi i(\boldsymbol{K}\cdot\boldsymbol{r}_j)\}},$$

where $\boldsymbol{K}$ is the scattering vector, $\boldsymbol{r}$ is the atomic position in the unit cell, and D is expressed as $D = \frac{e^2\gamma_N}{mc^2} = -0.539 \times 10^{-15}$ m,
($e = 1.602 \times 10^{-19}$ C : charge of an electron, $\gamma_N = 5.051 \times 10^{-27}$ J/T : magnetic moment of a neutron, $m = 9.109 \times 10^{-31}$ kg : mass of an electron, $c = 2.998 \times 10^8$ m/s^2 : velocity of light).

We describe the calculating method for the magnetic form factors based on the theoretical model of the orbital ordering. The calculation will be compared with the experimental results in Chap. 4.4.

The PND experiments were done for single crystals of $Y_{1-x}Ca_xTiO_3$ ($x = 0.05$, 0.10 and 0.15) with the typical sample size of about $3 \times 3 \times 6$ mm^3. We used the triple-axis spectrometer, TOPAN, installed at the beam port 6G of the JRR-3M reactor at JAERI, Tokai. The data were collected at 1.6 K under a magnetic field $B = 1$ T applied parallel to the easy magnetization axis of c-axis with the incident neutron energy of 32.4 meV (wave length $\lambda = 1.59$ Å).

3.5 Resonant x-ray scattering

Resonant x-ray scattering (RXS) is one of the techniques to observe the orbital ordered state [16]. This method was first applied to a manganite $La_{0.5}Sr_{1.5}MnO_4$ [18], and has been exploited to other $3d$ and $4f$ materials, e.g. $YTiO_3$ [19], $LaTiO_3$ [20], YVO_3 [21], V_2O_3 [22], NaV_2O_5 [23], $LaMnO_3$ [24], $La_{1-x}Sr_xMnO_3$ [25], $Pr_{1-x}Ca_xMnO_3$ [26], $Nd_{0.5}Sr_{0.5}MnO_3$ [27], $LaSr_2Mn_2O_7$ [28], Fe_3O_4 [29], $KCuF_3$ [30], DyB_2C_2 [31], CeB_6 [32], and UPd_3 [33].

In the RXS we make use of the anomalous scattering factor at the absorption-edge energy of the target atom in the system. Therefore, we obtain local information of the

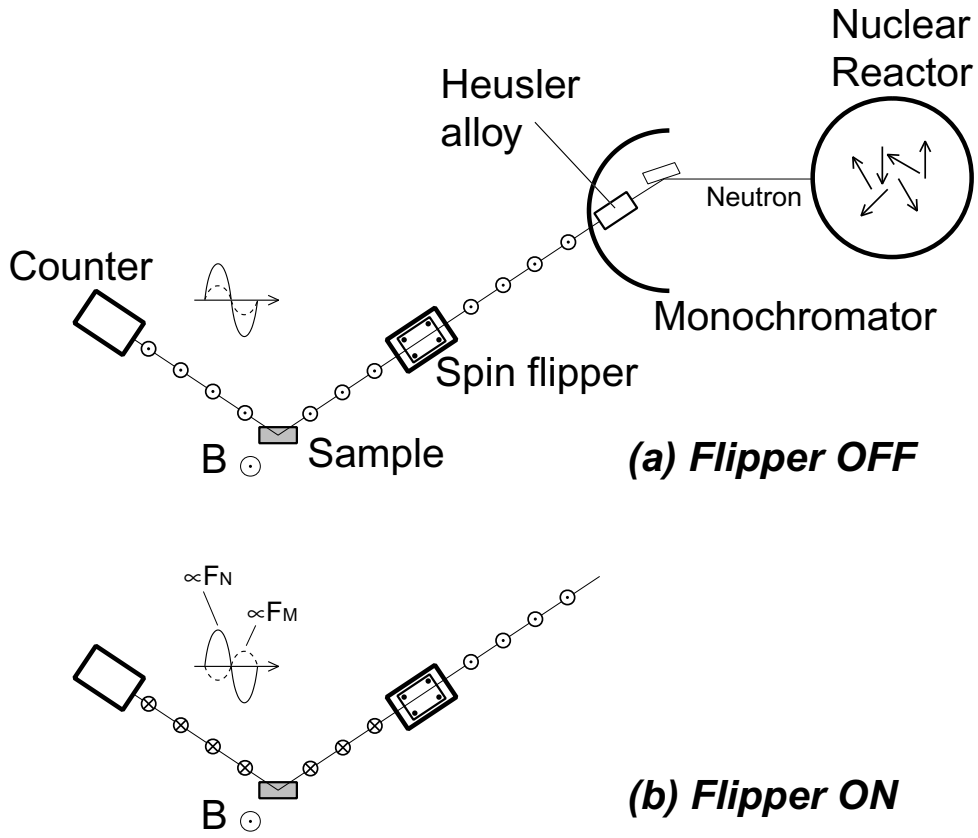

Figure 3.2: Schematic top views of the polarized neutron diffraction exprtiment. When the spin flipper is on, the spin direction of incident neutron beams turns from upside to down.

specific atom. In general, the x-ray diffraction intensity for (hkl) reflection $I(hkl)$ is expressed by using the crystal structure factor F_{hkl} as;

$$I(hkl) \propto |F_{hkl}|^2, \quad F_{hkl} = \sum_j f_j \exp\left(i\boldsymbol{k}_{hkl} \cdot \boldsymbol{r}_j\right),$$

where f is the atomic scattering factor, $\boldsymbol{k}_{hkl}$ is the scattering vector of the (hkl), and $\boldsymbol{r}$ is the atomic position in the unit cell. The atomic-scattering factor at the x-ray energy E near the absorption energy E_A is composed of three terms,

$$f(E) = f_0 + f'(E) + f''(E),$$

where f_0, f' and f'' are the normal Thomson scattering factor and real and imaginary parts of the anomalous scattering factor, respectively. It is noted that these anomalous scattering factor should be described as a *tensor* when the orbitals are ordered. Since the crystal structure factor is a *tensor*, the RXS intensity depends on both the azimuthal angle and polarization analyzer angle. The azimuthal angle Ψ is the angle around the scattering vector as shown in Fig. 3.3 The polarization analyzer angle ϕ is the angle of the scattered beam from the PG(0 0 4) analyzer crystal.

Here, we consider the case of $LaMnO_3$ with the antiferro orbital ordering, as shown in Fig. 3.4. In $LaMnO_3$, $Mn^{3+}(1)$ and $Mn^{3+}(2)$ are alternatively arranged with the $(3y^2 - r^2)$ and $(3x^2 - r^2)$ type orbitals, respectively, based on the xy-coordinates. The ordered orbitals of $Mn^{3+}(1)$ and $Mn^{3+}(2)$ are elongated to the direction of y and x, respectively. The atomic scattering tensors for each Mn site are expressed as the following, respectively,

$$\hat{f}_1 = \begin{pmatrix} f_\perp & 0 & 0 \\ 0 & f_\parallel & 0 \\ 0 & 0 & f_\perp \end{pmatrix}, \qquad \hat{f}_2 = \begin{pmatrix} f_\parallel & 0 & 0 \\ 0 & f_\perp & 0 \\ 0 & 0 & f_\perp \end{pmatrix}$$

where $f_\parallel$ and $f_\perp$ are the principal values of parallel and perpendicular to the direction of elongated $(3z^2 - r^2)$ type orbital, respectively. By taking account of the transformation introduced by the angular dependence around the scattering vector (azimuthal scan), we can calculate the azimuthal angle dependence of the orbital ordered superlattice intensity in the configuration shown in Fig. 3.3;

$$I(\theta, \Psi) \propto (f_\parallel - f_\perp)^2 \cos^2\theta \sin^2\Psi,$$

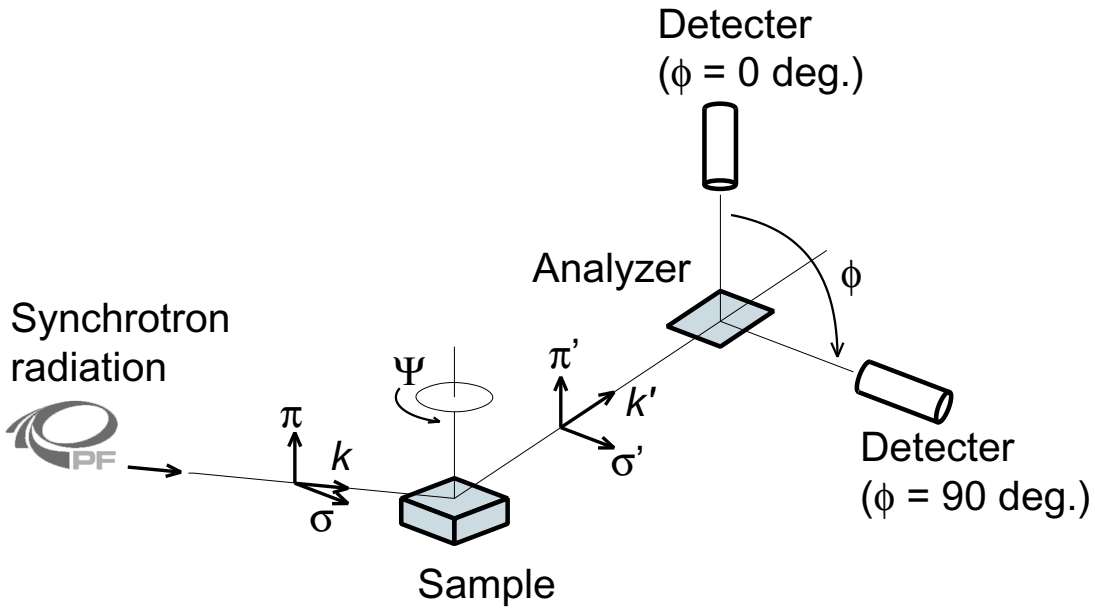

Figure 3.3: Schematic view of the RXS experimental configuration and definition of the polarization directions of x-ray at BL-16A2, Photon Factory, KEK. The polarization directions σ' and π' of scattered beam is perpendicular and parallel to the scattering plane, respectively.

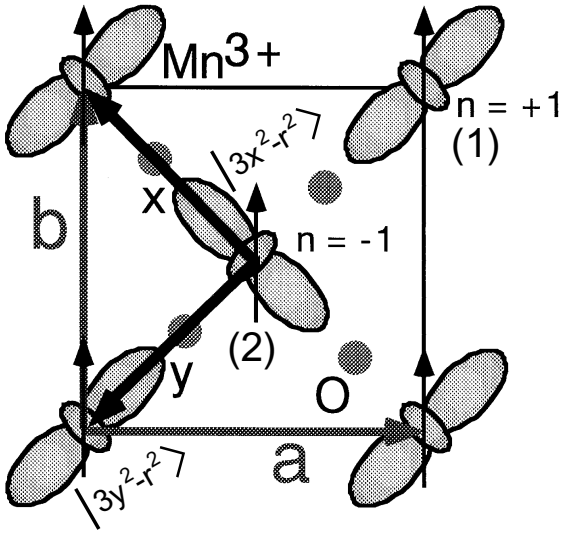

Figure 3.4: The orbital ordering in the *ab*-plane of the perovskite manganite, $LaMnO_3$. The orbital ordering along the *c* axis repeats the same pattern [24].

where θ is the Bragg angle of the orbital ordered superlattice. In the case of $Y_{1-x}Ca_xTiO_3$, the azimuthal dependence of the RXS intensities are quite complicated, because of having four Ti sites as shown in Fig. 3.5. If the antiferro orbital ordering proposed by Mizokawa *et al.* [34] is realized in $Y_{1-x}Ca_xTiO_3$, the azimuthal angle dependence of the (1 0 0) and (0 0 1) reflections should exhibit twofold symmetry. At the (0 1 1) reflection, on the other hand, the azimuthal angle dependence of the $\sigma \rightarrow \sigma'$ component would show a fourfold symmetry, while the $\sigma \rightarrow \pi'$ component has a period of 360°, where σ and π mean the directions of linear polarization perpendicular and parallel to the scattering plane.

For the measurements, samples were shaped into blocks with surfaces of (1 0 0), (0 0 1) and (0 1 1) of approximately 3×3 mm^2 and the surfaces were polished with Al_2O_3 powders of 1 μm. The full width at half maximum of the typical mosaic width was about 0.07°. The experiments were performed on a six-axes diffractometer at BL-16A2, Photon Factory, KEK. The incident x-ray was monochromatized by a flat double-crystal Si(1 1 1) monochromator and focused by a bent cylindrical mirror. The incident energy was tuned to the Ti K-edge, which was experimentally determined to be 4.966 keV from the fluorescence measurement. At this energy, the energy resolution was about 1 eV. To separate from the diffracted beam to the linearly polarized σ' and π' components, we used a PG(0 0 4) analyzer crystal as necessary, which gives a scattering angle of about 96° at this energy. The azimuthal angle and energy dependences of the RXS were measured at room temperature for all samples.

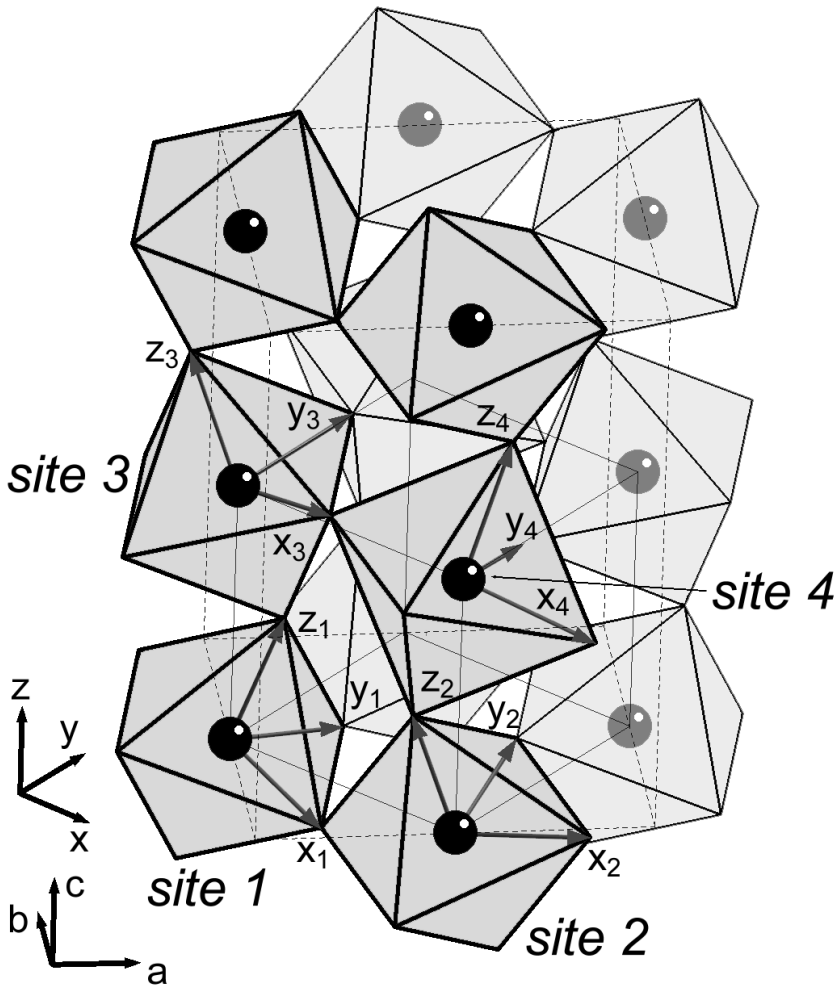

Figure 3.5: The crystal structure of $Y_{1-x}Ca_xTiO_3$ (Space Group : $Pbnm$), where oxygen ions are located at the apical of octahedrons. The dashed line represents the unit cell. Four Ti ions are at $(0, 1/2, 0)$, $(1/2, 0, 0)$, $(0, 1/2, 1/2)$ and $(1/2, 0, 1/2)$ for the sites 1, 2, 3 and 4, respectively. The quantum axes x_n, y_n, z_n $(n = 1 \sim 4)$ are defined from each titanium site toward the neighbouring oxygen ion.

Chapter 4

Results and discussion

4.1 Transport and magnetic properties

Figure 4.1(a) presents the temperature dependences of the electrical resistivity ρ for samples of $Y_{1-x}Ca_xTiO_3$ ($x = 0.3$, 0.37, 0.38, 0.39, and 0.41), where the electrical current direction is parallel to the orthorhombic a-axis.

With increasing x from 0 to 0.41, ρ at 300 K is decreased by four orders of magnitude, as can be seen in Table. 4.1. To examine the anisotropy of $\rho(T)$, we measured $\rho(T)$ for three current directions $I \parallel a$, $\parallel b$ and $\parallel c$. As a result, no systematic differences were observed.

The high-temperature semiconducting behavior of $\rho(T)$ is described by the Arrhenius' equation; $\rho(T) = \rho_1 \exp(E_g/2k_BT)$, where ρ_1, E_g and k_B are a coefficient, an energy gap and the Boltzmann constant, respectively. The values of E_g are listed in Table. 4.1, and plotted as a function of x in Fig. 4.2. On cooling below $\sim$ 200 K, $\rho(T)$ for $x =$ 0.38 and 0.39 shows a sharp peak which is followed by a drastic decrease. The thermal hysteresis is characteristic of a first order transition, which is coupled with lattice degree of freedom such as the phase transition and the phase separation [3]. With increasing x, the hysteresis width gradually decreases. As for the MI transition temperature, T_ρ, we took the temperature where the data of $\rho(T)$ on heating has the maximum. Thus determined T_ρ's are 85, 145 and 165 K for $x = 0.37$, 0.38 and 0.39, respectively. The ratio $\rho(T_\rho)/\rho(4.2\text{K})$ for $x = 0.39$ is $\sim 10^4$, which is larger by two orders of magnitude

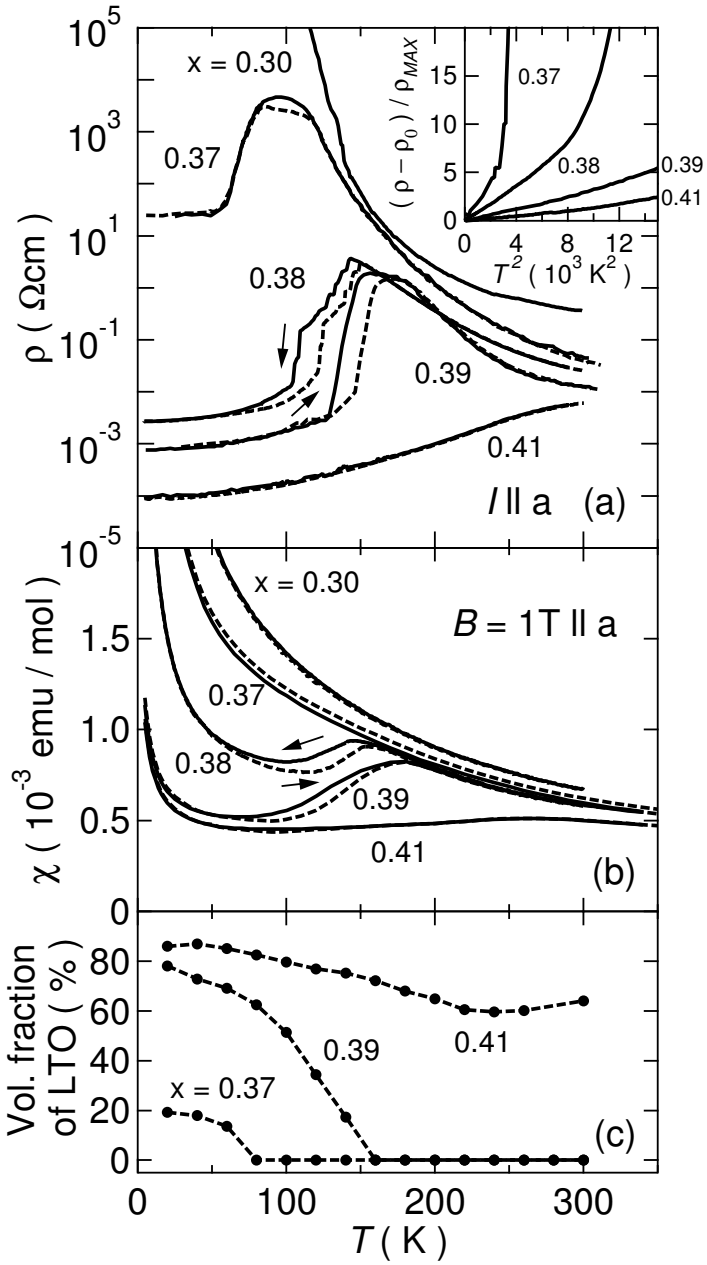

Figure 4.1: Temperature dependences of (a) electrical resistivity, (b) magnetic susceptibility and (c) volume fraction of the low-temperature orthorhombic phase in $Y_{1-x}Ca_xTiO_3$. Dashed and solid lines show heating and cooling processes, respectively. The inset shows the normalized resistivity $(\rho - \rho_0)/\rho_{\rm MAX}$ vs T^2, where ρ_0 is the residual resistivity and $\rho_{\rm MAX}$ is the maximum value at temperatures below 300 K. The data for $x = 0.38$, 0.39 and 0.41 are multiplied by 10000, 10000 and 100, respectively.

than that reported for polycrystalline samples [3, 4, 40–43]. For $x = 0.41$, by contrast, $\rho(T)$ shows a metallic behavior without hysteresis in the whole temperature region. At low temperatures, $\rho(T)$ for all samples obeys the T^2-law, $\rho = \rho_0 + AT^2$ as was observed in polycrystalline samples [3, 43, 44]. The residual resistivity ρ_0 decreases from 25 Ωcm for $x = 0.37$ to 10^{-4} Ωcm for $x \geq 0.39$.

Table 4.1: Parameters to describe the electrical resistivity $\rho(T)$ of $Y_{1-x}Ca_xTiO_3$. At low temperatures, $\rho(T)$ obeys the T^2 law, $\rho(T) = \rho_0 + AT^2$. Above T_ρ, $\rho(T)$ obeys the activation law with the energy gap E_g.

x	ρ(300K) (Ωcm)	ρ_0 (Ωcm)	A (Ωcm/K^2)	T_ρ (K)	E_g (K)
0.0	3.2×10^{1}	—	—	—	4800
0.10	8.7×10^{0}	—	—	—	2640
0.20	1.7×10^{0}	—	—	—	2040
0.30	3.5×10^{-1}	—	—	—	1130
0.37	3.6×10^{-2}	2.45×10^{1}	1.19×10^{-3}	85	3600
0.38	2.9×10^{-2}	2.64×10^{-3}	2.74×10^{-7}	145	2560
0.39	1.3×10^{-2}	6.87×10^{-4}	1.02×10^{-8}	165	1600
0.41	6.1×10^{-3}	8.46×10^{-5}	7.35×10^{-9}	—	—

First, we discuss the hole-doping effect on $\rho(T)$. A simple picture for the MI transition based on the Mott-Hubbard model is as following. If x holes per formula unit are doped, the number of $3d$ electrons per Ti ion n would decrease as $n = 1 - x$. At a small x, say 0.05 as was observed in $La_{1-x}Sr_xTiO_3$ [39], the holes produced in the lower Hubbard band would become mobile, then the insulating state changes to a metallic state. However, the transition in $Y_{1-x}Ca_xTiO_3$ occurs at a large value $x = 0.39$, as shown in Fig. 4.1. For the insulating phase, the energy gap E_g estimated from $\rho(T)$ is listed in Table. 4.1. The magnitude of E_g as a function of x decreases linearly for $0.37 \leq x \leq 0.39$, and the linear extrapolation of $E_g(x)$ to larger x region leads to a critical concentration $x_c^h = 0.405$ where E_g vanishes. At $x = 0.41$ just above x_c^h, in fact, a metallic state is stabilized even at 290

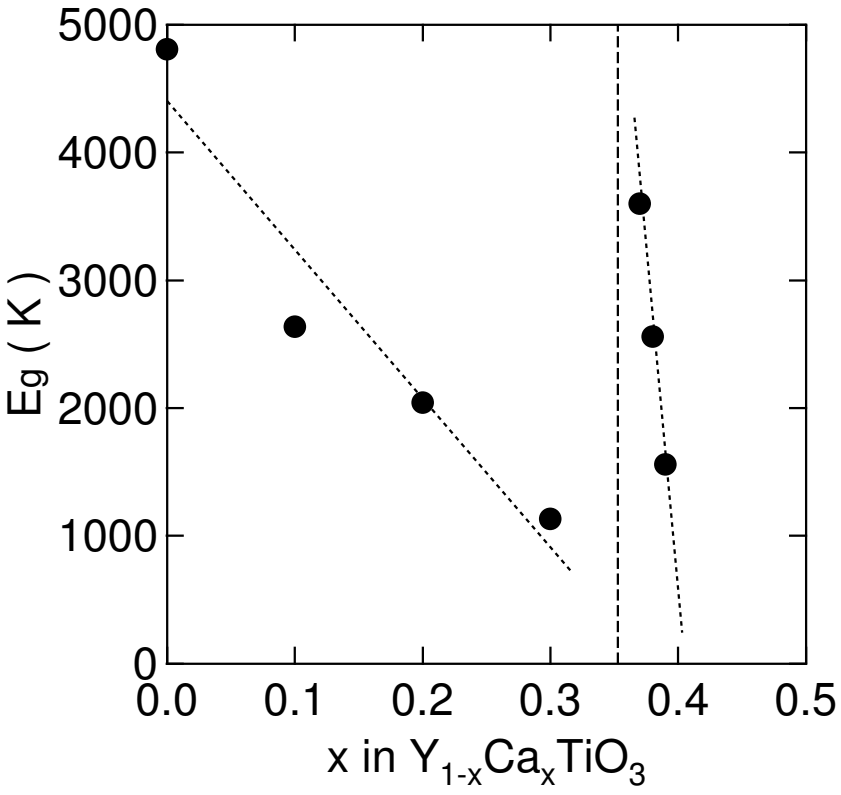

Figure 4.2: x dependences of the energy gap E_g.

K.

In Fig. 4.1(b), we show the temperature dependences of magnetic susceptibility $\chi(T)$ of selected samples under a magnetic field of 1 T applied parallel to the a axis. No anisotropy in $\chi(T)$ was observed, for all paramagnetic samples with x in the range $0.3 \leq x \leq 0.41$. $\chi(T)$ for $T > 200$ K obeys the Curie-Weiss law, $\chi(T) = C^h/(T - \theta_p^h)$, where C^h is the Curie constant and θ_p^h is the Weiss temperature. The parameters obtained by a least squares fit are listed in Table. 4.2. The effective magnetic moment $\mu_{\rm eff}$ was evaluated from; $\mu_{\rm eff} = \sqrt{3k_B C^h/N_A}$, where N_A is the Avogadro's number. In order to describe the data of $\chi(T)$ below 50 K for $0.37 \leq x \leq 0.41$, the inclusion of the temperature independent term was necessary, *ie*, $\chi(T) = \chi_0^\ell + C^\ell/(T - \theta_p^\ell)$, where χ_0^ℓ originates from diamagnetic and Pauli paramagnetic contributions. For $x = 0.37$, no peak appears in $\chi(T)$, even though $\rho(T)$ has a broad peak at $T_\rho = 100$ K. For $x = 0.38$ and 0.39, a broad peak appears in $\chi(T)$ at $T_\chi = 170$ K and 180 K, respectively. The values of T_χ are almost same as those of T_ρ.

We pay our attention to the metallic phase at low temperatures, where $\rho(T)$ follows the T^2 law. From the values of the residual resistivity ρ_0 and coefficient A listed in Table. 4.1, one notices that both A and ρ_0 rapidly decrease by four orders of magnitude between $x = 0.37$ and 0.38. In order to consider the reason for the large drop of ρ_0, we recall that the metallic LTO phase appears at 100 K and 150 K for $x = 0.37$ and 0.39, respectively [45]. For $x = 0.41$, however, the volume fraction of the LTO phase is 60% at room temperature. The volume fraction of the LTO phase increases on cooling and saturates to 20, 80 and 90% for $x = 0.37$, 0.39 and 0.41, respectively. By comparing the results of $\rho(T)$ and the volume fraction for $x = 0.39$ in Figs. 4.1(a) and 4.1(c), we find that the $\rho(T)$ starts to drop when the LTO phase appears. When the volume fraction of the LTO phase is saturated, then $\rho(T)$ obeys the T^2 law.

In certain manganites and cuprates, phase separations into metallic and insulating domains are known to be responsible for the transition from an insulating state to a metallic state [49]. Monte Carlo simulations of $\rho(T)$ for such systems using two or three dimensional clusters indicated that the resistivity behaves metallic when the volume fraction of metallic phase amounts to $20 \sim 30\%$ [50–52]. In the present system $Y_{1-x}Ca_xTiO_3$, the

percolation of the metallic LTO phase may lead to the metallic behavior in $\rho(T)$.

We discuss the hole-doping effect on $\chi(T)$ by analyzing the parameters listed in Table. 4.2. At high temperatures, where the whole sample is in a single phase of the high-temperature orthorhombic, $\chi(T)$ obeys a Curie-Weiss law, $\chi(T) = C^h/(T-\theta_p^h)$. By using the Curie constant C^h, the effective magnetic moment $\mu_{\rm eff}$ per Ti atom was evaluated as $\mu_{\rm eff}^h = \sqrt{3k_B C^h/N_A}$. Based on the assumption of the valence states $Y_{1-x}^{3+}Ca_x^{2+}(Ti_{1-x}^{3+}Ti_x^{4+})O_3$, on the other hand, the average spin moment μ_s per Ti atom is calculated as $\mu_s = \sqrt{1-x} \times 2\sqrt{S(S+1)}$, where $S = 1/2$ for the Ti^{3+} ion. From the values of $\mu_{\rm eff}^h$ and μ_s, the ratio $\mu_{\rm eff}^h/\mu_s$ was evaluated and listed in Table. 4.2. The fact that the ratio is nearly 1 in the whole range of $0 \leq x \leq 0.39$ confirms that x holes per formula unit is really doped by the Ca substitution in the insulating region. In the metallic region $x \geq 0.4$, the doped hole x corresponds to the carrier number, $n = 1 - x$, which was first pointed out from the x dependence of the Hall coefficient [4].

Table 4.2: Parameters to describe the magnetic susceptibility $\chi(T)$ of $Y_{1-x}Ca_xTiO_3$. T_χ is the peak temperature. μ_s is the average spin moment per Ti atom evaluated by the localized spin model. $\chi(T)$ for $T < 50$ K obeys a modified Curie-Weiss law, $\chi(T) = \chi_0^\ell + C^\ell/(T - \theta_p^\ell)$. At temperatures above T_χ, $\rho(T)$ obeys a Curie-Weiss law, $\chi(T) = C^h/(T - \theta_p^h)$. The effective spin moment per Ti atom $\mu_{\rm eff}$ is calculated from $\mu_{\rm eff} = \sqrt{3k_BC/N_A}$.

x	T_χ	χ_0^ℓ	C^ℓ	θ_p^ℓ	$\mu_{\rm eff}^\ell$	C^h	θ_p^h	$\mu_{\rm eff}^h$	μ_s.$\mu_{\rm eff}^h/\mu_s$
	(K)	(10^{-4} emu/mol)	(emuK/mol)	(K)	($\mu_{\rm B}$)	(emuK/mol)	(K)	($\mu_{\rm B}$)	($\mu_{\rm B}$).
		$2 < T < 50$ K				$T_\chi < T < 350$ K			
0.0	—	—	—	—	—	0.375	29.8	1.73	1.73. 1.00
0.10	—	—	—	—	—	0.316	22.0	1.59	1.64. 0.97
0.20	—	—	—	—	—	0.298	7.5	1.54	1.55. 0.99
0.30	—	—	—	—	—	0.257	-1.7	1.43	1.45. 0.97
0.37	—	8.48	0.0414	-2.46	0.18	0.239	-10.8	1.38	1.37. 1.01
0.38	150	7.46	0.0162	-2.39	0.070	0.236	-38.0	1.37	1.36. 1.01
0.39	175	4.25	0.00566	-2.55	0.025	0.229	-49.4	1.35	1.35. 1.00
0.41	250	3.78	0.00512	-2.46	0.023	—	—	—	1.33. —

At temperatures below 50K, the samples for $x \geq 0.37$ are decomposed into the monoclinic and the LTO phases. When the volume fraction of the LTO is saturated, $\chi(T)$ obeys a modified Curie-Weiss low, $\chi(T) = \chi_0^\ell + C^\ell/(T - \theta_p^\ell)$. In Table. 4.2, the parameters χ_0^ℓ, C^ℓ, θ_p^ℓ and $\mu_{\rm eff}^\ell$ are listed. It should be noted that the values of $\mu_{\rm eff}^\ell/\mu_{\rm eff}^h$ are 0.17, 0.069 and 0.025 for $x = 0.37$, 0.38 and 0.39, respectively. This significant decrease in $\mu_{\rm eff}^\ell/\mu_{\rm eff}^h$ below 1 can be understood if the size of localized moments in the insulating phase above T_ρ is reduced in the monoclinic phase below T_ρ. On going from $x = 0.37$ to 0.41, the value of χ_0^ℓ is decreased to less than half. This x dependence of χ_0^ℓ can be smoothly connected to the previous result for $x \geq 0.4$ [3,39]. This drop in χ_0^ℓ for $x \geq 0.4$ indicates the reduction in the electron correlation as the system changes into the metallic phase.

Figure 4.1(c) represents the temperature dependences of the volume fraction of the LTO phase estimated from powder x-ray diffraction analysis [45]. To compare T_ρ and the phase separation temperature $T_{\rm PS}$, we define $T_{\rm PS}$ as the temperature in which the volume fraction of LTO is 10% of its saturated value. The values of $T_{\rm PS}$ are plotted as a function of x in Fig. 4.5. These are same as those of T_ρ.

4.2 Pressure effects on structural and transport properties

The previous study of pressure effect on the MI transition in polycrystalline samples of $Y_{1-x}Ca_xTiO_3$ ($x = 0.375$, 0.39 and 0.40) showed that application of pressure of about 1 GPa changes the system into a metallic state [4,47,48]. For comparison, we have chosen single crystalline samples with $x = 0.37$ and 0.39 for the resistivity measurements under pressure. Here, it should be noted that the samples were cut from a different rod from that used for the measurements of $\rho(T)$ and $\chi(T)$ under ambient pressure.

Figure 4.3 represents the results of $\rho(T)$ under various pressures for $x = 0.39$. The sharp transition at $T_\rho = 165$ K under ambient pressure is changed to a gradual transition at a low pressure of 0.16 GPa. Because no maximum is observed, we take for convenience the transition inflection point in the $\rho(T)$ curve as the temperature $T_\rho(P)$. Upon increasing pressure up to 0.96 GPa, T_ρ increases and the value of $\rho(T = 280$ K) decreases by one

order of magnitude. It is noteworthy that in the metallic state below 150 K, $\rho(T)$ does not depend on pressure, and obeys the T^2-law below 70 K. The overall temperature dependence at $P = 0.96$ GPa resembles that for $x = 0.41$ at $P = 0$ GPa shown in Fig. 4.1(a).

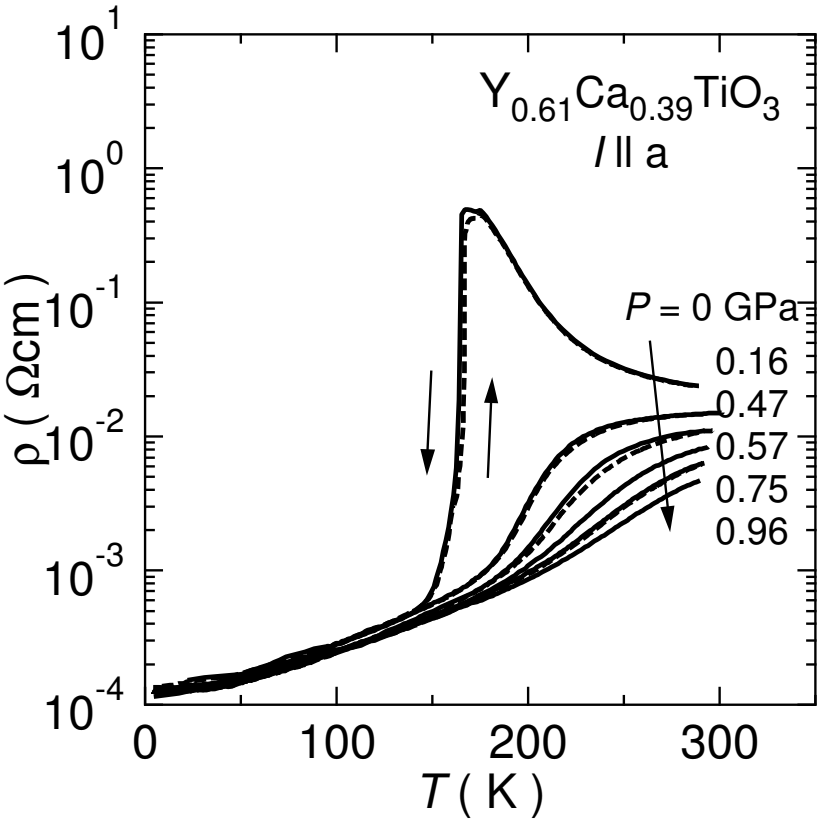

Figure 4.3: Temperature dependences of electrical resistivity in $Y_{0.61}Ca_{0.39}TiO_3$ under various constant pressures up to 1 GPa. Dashed and solid lines show heating and cooling processes, respectively. Above 150 K, $\rho(T)$ rapidly decreases with increasing pressure and shows a metallic behavior, while $\rho(T)$ is almost independent of pressure below 150 K.

For the sample of $x = 0.37$, we show in Fig. 4.4 the temperature dependences of $\rho(T)$ and volume fraction of the LTO phase under various pressures. For the resistivity measurements, we used a clamp-type piston-cylinder pressure cell, in which the pressure decreased by about 0.1 GPa on cooling due to the solidification of the pressure transmitting medium. The correction of the pressure value was made by using the known pressure

dependence of resistance in a manganin wire [46]. In Fig. 4.4(a), the pressure value estimated at T_ρ in the heating process is noted. Upon increasing pressure, T_ρ increases steadily, while the residual resistivity ρ_0 decreases by three orders of magnitude in the narrow range $0.44 \leq P \leq 0.58$ GPa. It should be noted that the sharp transition in $\rho(T)$ at 0.84 GPa is similar to that of $x = 0.39$ at $P = 0$ (see Fig. 4.3). The width of hysteresis decreases and vanishes at $P = 1.2$ GPa. At higher pressures, the system behaves metallic in the whole temperature region, and $\rho(T)$ obeys the T^2-law below 70 K.

The volume fraction of the LTO phase under pressure was estimated by powder x-ray diffraction experiments with the method described in Chapter 4.1. At $P = 0$, the LTO phase appears below 120 K, and the volume fraction increases on cooling and saturates to a value of 25% of the whole sample. We define the phase separation temperature $T_{\rm PS}$ by the same way as at ambient pressure. With increasing pressure up to 0.8 GPa, both $T_{\rm PS}$ and the volume fraction increase. At $P = 1.7$ GPa, $T_{\rm PS}$ eventually exceeds 300 K and the LTO phase is stabilized in the whole volume.

In this section, we compare the hole-doping effect with the pressure effect on both the MI transition and the phase separation in $Y_{1-x}Ca_xTiO_3$. In Fig. 4.5, we represent four sets of data of characteristic temperatures; the pressure dependence of T_ρ and $T_{\rm PS}$ for $x = 0.37$, the pressure dependence of T_ρ for $x = 0.39$, and x dependence of T_ρ for $0.37 \leq x \leq 0.41$ at ambient pressure. Here, the origin at $P = 0$ for $x = 0.39$ is shifted upward by 0.82 GPa with respect to that for $x = 0.37$ so that the curve of $T_\rho(P)$ for $x = 0.39$ lies on the curves of $T_\rho(P)$ and $T_{\rm PS}(P)$ for $x = 0.37$. This agreement between the two sets of data implies that the effect of hole-doping of Ca 2% on the MI transition corresponds to that of application of pressure of 0.82 GPa. This correspondence can be used to normalize the horizontal scale x in order to plot the data of $T_\rho(x)$ for $0.37 \leq x \leq 0.41$ together in Fig. 4.5. Now, all the data of $T_\rho(P)$, $T_{\rm PS}(P)$ and $T_\rho(x)$ agree well. Thus, both hole-doping and application of pressure have equivalent effects on both the MI transition and the phase separation in $Y_{1-x}Ca_xTiO_3$. Similar correspondence was reported in another titanate $LaTiO_{3+\delta}$ and in a manganite $La_{1-x}Sr_xMnO_3$, where both hole-doping and application of pressure stabilize the metallic state as a common result of the decrease in the ratio U/t [53, 54].

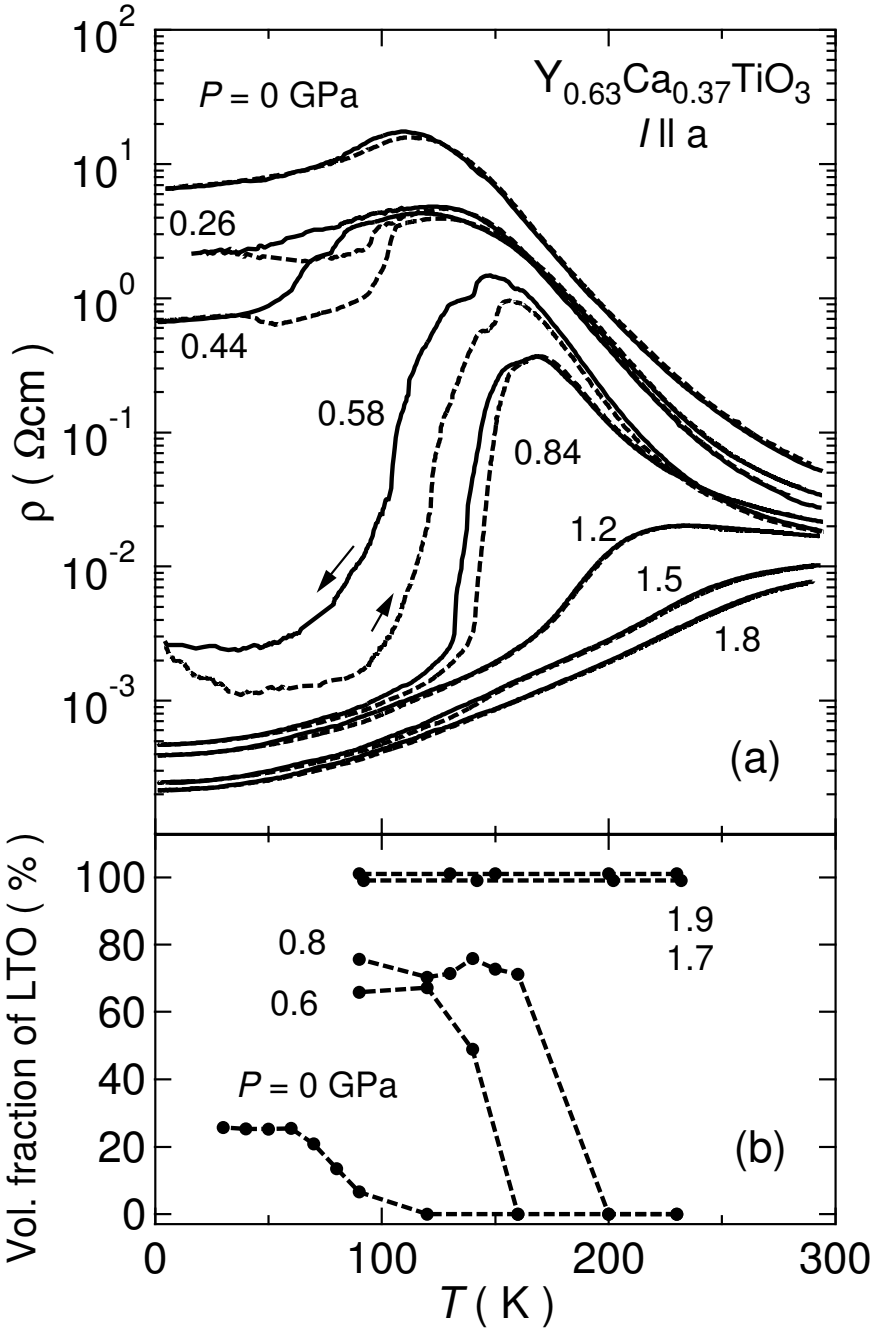

Figure 4.4: Temperature dependences of (a) electrical resistivity and (b) volume fraction of the LTO phase in $Y_{0.63}Ca_{0.37}TiO_3$ under pressures up to ~ 2 GPa. Dashed and solid lines show heating and cooling processes, respectively.

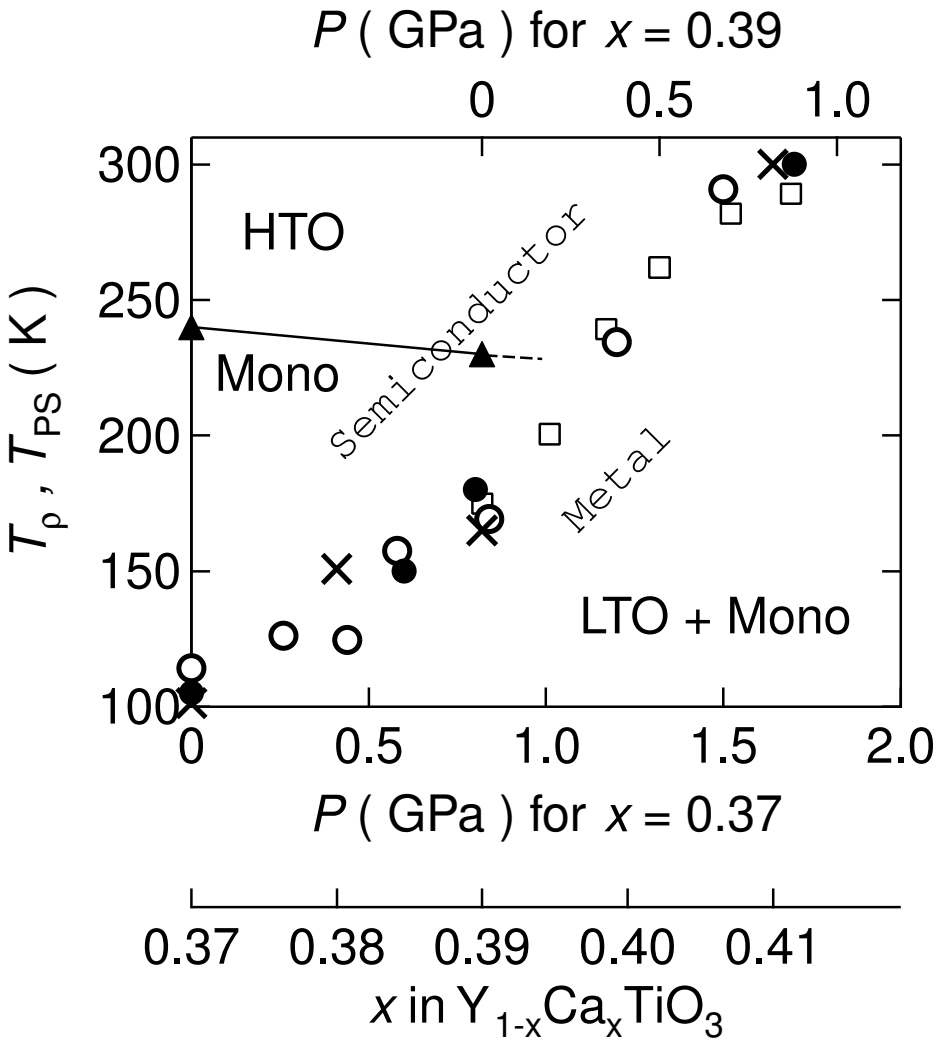

Figure 4.5: Pressure dependences of $T_\rho(P)$ and $T_{\rm PS}(P)$ for $x = 0.37$ and 0.39, and x dependences of T_ρ at ambient pressure for $Y_{1-x}Ca_xTiO_3$. Open (○) and closed (●) circles show $T_\rho(P)$ and $T_{\rm PS}(P)$ for $x = 0.37$, respectively. Open squares (□) represent $T_\rho(P)$ for $x = 0.39$, and the zero point of $T_\rho(P)$ for $x = 0.39$ is shifted by 0.82 GPa higher than that of $T_\rho(P)$ for $x = 0.37$. Crosses (×) show x dependence of T_ρ at ambient pressure in $Y_{1-x}Ca_xTiO_3$. Closed triangles (▲) represent the temperature of the phase transition from the high temperature orthorhombic phase (HTO) to the monoclinic one.

Powder x-ray diffraction analysis has shown that the MI transition in $Y_{1-x}Ca_xTiO_3$ is a result of percolation of the metallic LTO domains. In Fig. 4.5, the linear extrapolation of the data of $T_\rho(x)$ and $T_{\rm PS}(x)$ to smaller x region leads to the lower critical concentration $x_c \sim 0.33$ where $T_\rho(x)$ or $T_{\rm PS}(x)$ vanishes. This fact suggests that the phase separation and MI transition may remain until x is decreased to $x = 0.33$ at ambient pressure. This critical concentration is much larger than $x_c = 0.05$ for a typical Ti-based Mott transition system $La_{1-x}Sr_xTiO_3$ [39].

One possible reason for the large difference in the critical concentration between 0.33 in $Y_{1-x}Ca_xTiO_3$ and 0.05 in $La_{1-x}Sr_xTiO_3$ is the difference in the charge gap in the host compounds. The Mott-Hubbard gap of $YTiO_3$ is of 1 eV. On the other hand, that of $LaTiO_3$ is of 0.1 eV [3, 55]. Another reason may be the orbital ordering in the former. It is known that the mother material $LaTiO_3$ for $La_{1-x}Sr_xTiO_3$ is an antiferromagnetic insulator without orbital ordering, then a metallic state is easily realized by hole-doping at a low level [56]. In contrast, the mother material $YTiO_3$ for $Y_{1-x}Ca_xTiO_3$ is a ferromagnetic insulator with orbital ordering, then the insulating state might be stable as long as the orbital order remains [8, 13, 14, 19]. If this is the case, the orbital ordered state may remain up to $x = 0.33$. To observe the orbital ordered state in the present system, polarized neutron diffraction and resonant x-ray scattering experiments have been performed. These results are described and discussed in Chapter 4.4 and 4.5.

4.3 Rietveld analysis of powder x-ray diffraction

The powder diffraction patterns of YCa_xTiO_3 were analyzed with the Rietveld method by using the program RIETAN-2000 [12] for $x = 0$, 0.05, 0.1, 0.15, 0.2, 0.3, 0.38, 0.5, 0.75 and 1 at room temperature. The results of the analysis are summarized in Table. 4.3. For all x except $x = 0.38$, the value of the goodness-of-fit indicator $S = R_{\rm wp}/R_{\rm e}$ are less than 1.3, where $R_{\rm wp}$ and $R_{\rm e}$ is a weighted pattern R-factor and an expected R-factor, respectively. $R_{\rm rp}$ and $R_{\rm e}$ is expressed as,

$$R_{\rm wp} = \left(\frac{\Sigma_i w_i [y_i - f_i(\boldsymbol{x})]^2}{\Sigma_i w_i y_i^2} \right)^{1/2}, \qquad R_{\rm e} = \left(\frac{N_{\rm p} - N_{\rm r} - N_{\rm c}}{\Sigma_i w_i y_i^2} \right)^{1/2},$$

where y_i, $f_i(\boldsymbol{x})$, $w_i (= 1/y_i)$, $N_{\rm p}$, $N_{\rm r}$, and $N_{\rm c}$ is the measured intensity at the diffraction angle $2\theta_i$, a calculated intensity, statistical weight of the data, the number of data of the measured intensities, the number of the fineness parameters and the number of conditions, respectively. The space group was assigned to $Pbnm$ for all data. This implies that there is no structural phase transition from $x = 0$ to 1 at room temperature within our experimental accuracy.

The bond angles of Ti-O-Ti; $\Theta_{\rm In}$ (along ab-plane) and $\Theta_{\rm Out}$ (along c-axis), the bond lengths of Ti-O; Ti-O_x, Ti-O_y and Ti-O_z, the ratios of Ti-O (Jahn Teller distortion); $\Delta^x_{\rm JT}$ = Ti-O_x/Ti-O_z and $\Delta^y_{\rm JT}$ = Ti-O_y/Ti-O_z and the bond angles between local coordination axes of O-Ti-O; O_x-Ti-O_y ($\angle(xy)$), O_y-Ti-O_z ($\angle(yz)$) and O_z-Ti-O_x ($\angle(zx)$) estimated from structural parameters are listed in Table. 4.4. Here, the local coordination axes x, y and z are along the Ti-O bond directions near $[1\bar{1}0]$, [110] and [001] as shown in Fig. 3.5. Suffix x, y and z means this local coordination axes at site 1 and 3. For the site 2 and 4, the suffix x is exchanged for y. Ti-O_x, Ti-O_y and Ti-O_z in TiO_6 octahedra is defined as the bond length between Ti and O as shown in Fig. 4.7 (a). As shown in Fig 4.6, $\Theta_{\rm In}$ and $\Theta_{\rm Out}$ denote in-plane (ab-plane) Ti-O-Ti angle and out-of-plane Ti-O-Ti angle which is along c axis, respectively. Fig. 4.7 (b) shows the bond angles of O-Ti-O; $\angle(xy)$, $\angle(yz)$ and $\angle(zx)$. $\Delta^x_{\rm JT}$ and $\Delta^y_{\rm JT}$ are defined as the ratio between the equatorial Ti-$O_{\rm E}$ and the apical Ti-O_z bond lengths, where E = x and y.

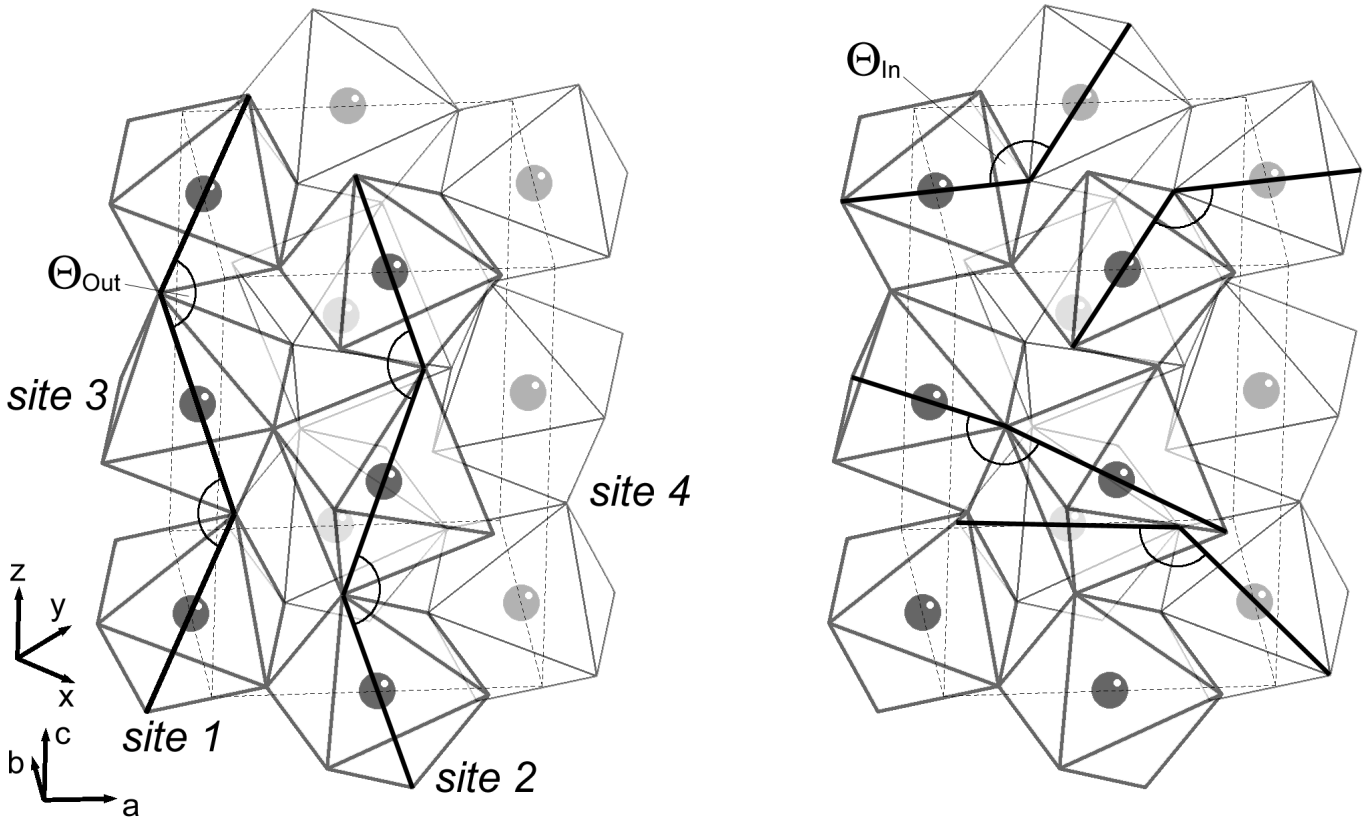

Figure 4.6: The bond angles of Ti-O-Ti; Θ_{Out} and Θ_{In}

.

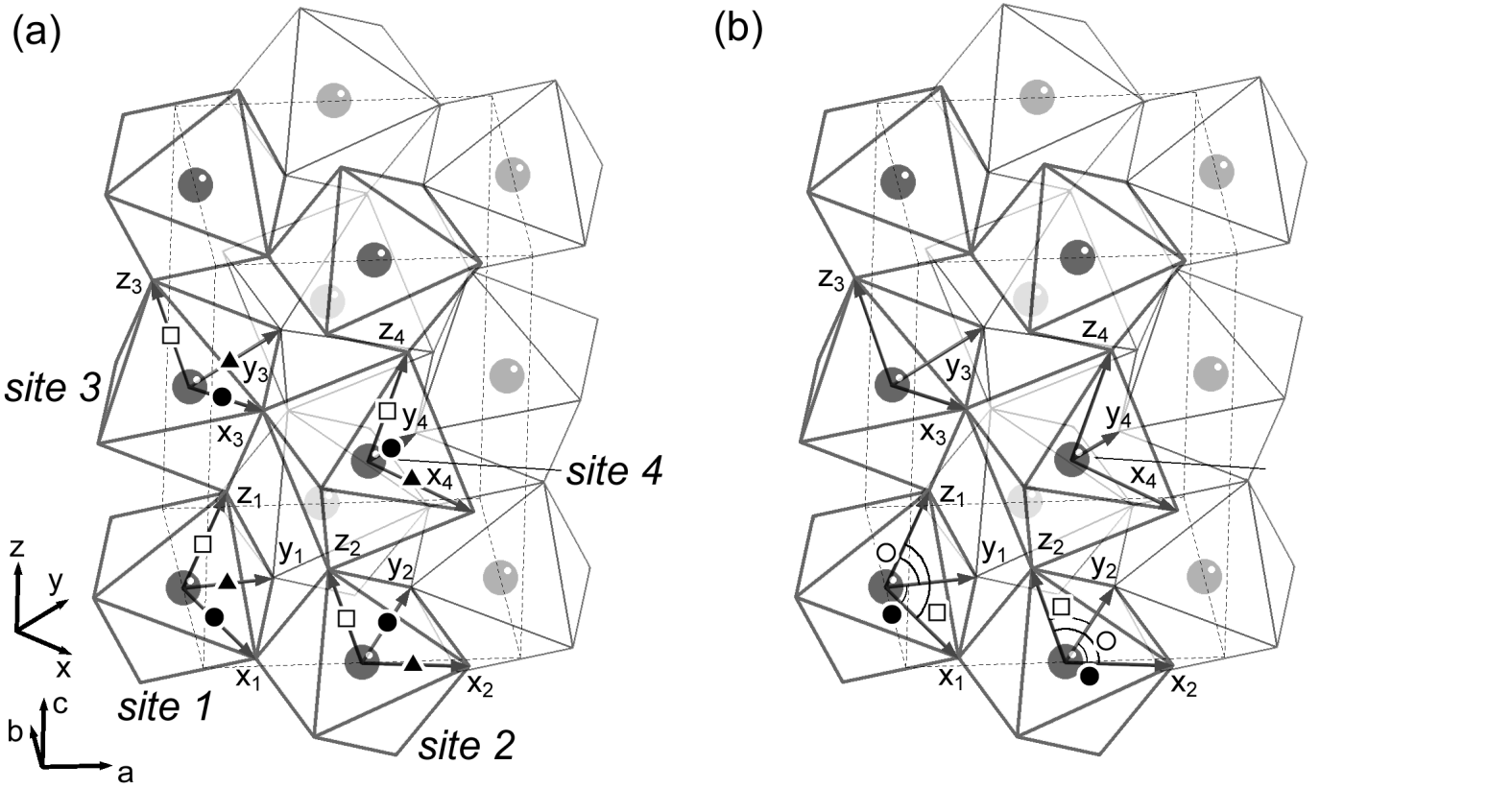

Figure 4.7: (a) The bond lengths of Ti-O. Closed circles (•), triangles (▲) and squares (□) show ,respectively. (b) The bond angles of O-Ti-O. Closed circles (•), open circles (○) and squares (□) show $\angle(xy)$, $\angle(yz)$ and $\angle(zx)$, respectively.

Table 4.3: Lattice constants and atomic positions for $Y_{1-x}Ca_xTiO_3$ at room temperature. In the space group $Pbnm$, Ti sits at (1/2, 0, 0), Y,Ca at (x, y, 1/4), O(1) at (x, y, 1/4) and O(2) at (x, y, z), respectively. R_{wp} is a weighted pattern R-factor and R_e is an expected R-factor. $S = R_{wp}/R_e$ is the goodness-of-fit indicator

x		0	0.05	0.1	0.15	0.2	0.3	0.38	0.5	0.75	1
a (Å)		5.3376(2)	5.3403(3)	5.3454(2)	5.3497(2)	5.3503(2)	5.3544(2)	5.3567(1)	5.3563(2)	5.3673(2)	5.3810(3)
b (Å)		5.6827(2)	5.6701(4)	5.6559(3)	5.6400(3)	5.6249(2)	5.6011(2)	5.5731(2)	5.5394(2)	5.4820(3)	5.4445(4)
c (Å)		7.6147(3)	7.6222(3)	7.6346(2)	7.6468(2)	7.6476(2)	7.6567(2)	7.6586(1)	7.6582(2)	7.6524(2)	7.6484(2)
Y,Ca	x	0.5199(3)	0.5196(6)	0.5184(4)	0.5171(4)	0.5168(4)	0.5160(6)	0.5142(3)	0.5128(5)	0.5100(6)	0.5068(7)
	y	0.5724(2)	0.5711(3)	0.5697(2)	0.5683(2)	0.5677(2)	0.5653(3)	0.5614(1)	0.5590(2)	0.5463(3)	0.5336(3)
O(1)	x	0.1213(14)	0.1157(23)	0.1154(17)	0.1150(16)	0.1149(16)	0.1087(18)	0.1049(9)	0.1005(14)	0.0816(15)	0.0703(16)
	y	0.4583(13)	0.4595(20)	0.4614(15)	0.4644(13)	0.4662(13)	0.4663(16)	0.4684(7)	0.4704(11)	0.4777(11)	0.4824(11)
O(2)	x	0.3088(9)	0.3085(15)	0.3088(11)	0.3085(11)	0.3091(10)	0.3086(13)	0.3049(6)	0.3045(9)	0.2972(9)	0.2914(9)
	y	0.6909(10)	0.6893(15)	0.6912(11)	0.6930(10)	0.6941(10)	0.6961(10)	0.7005(6)	0.7024(9)	0.7046(9)	0.7088(9)
	z	0.5570(8)	0.5576(13)	0.5570(9)	0.5560(9)	0.5565(8)	0.5541(13)	0.5508(5)	0.5481(8)	0.5387(9)	0.5354(8)
R_{wp} (%)		4.81	5.53	3.90	4.81	3.02	3.31	3.48	3.96	5.06	3.94
R_e (%)		4.58	4.36	4.09	3.68	3.10	3.22	1.56	2.92	3.87	4.85
S		1.05	1.27	0.95	1.31	0.97	1.03	2.23	1.36	1.31	0.81

Table 4.4: Structural parameters for $Y_{1-x}Ca_xTiO_3$ at room temperature.

x	0	0.05	0.1	0.15	0.2	0.3	0.38	0.5	0.75	1
Θ_{In} (deg)	144.1(15)	143.7(15)	144.1(15)	144.6(15)	144.5(15)	145.5(16)	147.7(16)	148.7(16)	152.9(16)	155.5(17)
Θ_{Out} (deg)	140.2(10)	141.8(10)	142.1(10)	142.6(10)	142.9(10)	144.5(10)	145.9(10)	147.6(10)	153.3(10)	156.9(10)
Ti-O_x (Å)	2.077(4)	2.084(5)	2.070(4)	2.057(5)	2.050(4)	2.030(5)	2.008(2)	1.991(4)	1.974(4)	1.961(3)
Ti-O_y (Å)	2.021(4)	2.015(5)	2.020(4)	2.023(4)	2.026(4)	2.027(5)	2.016(2)	2.010(4)	1.972(4)	1.955(3)
Ti-O_z (Å)	2.025(2)	2.016(2)	2.018(2)	2.018(2)	2.017(2)	2.010(2)	2.003(1)	1.994(1)	1.966(1)	1.951(1)
Δ^x_{JT}	1.026(2)	1.034(4)	1.026(3)	1.019(3)	1.016(3)	1.010(3)	1.002(1)	0.998(3)	1.004(3)	1.005(2)
Δ^y_{JT}	0.998(3)	1.000(3)	1.001(3)	1.002(3)	1.004(3)	1.008(3)	1.006(2)	1.008(3)	1.003(3)	1.002(2)
O_x-Ti-O_y (deg)	90.5(12)	90.2(12)	90.2(12)	90.1(12)	90.0(12)	90.1(12)	90.1(13)	90.1(13)	89.9(13)	89.5(14)
O_y-Ti-O_z (deg)	90.2(15)	90.9(15)	90.7(15)	90.3(15)	90.2(15)	90.5(15)	90.4(16)	90.2(16)	90.1(17)	90.5(17)
O_z-Ti-O_x (deg)	93.4(14)	92.7(14)	92.5(14)	92.2(14)	91.8(14)	91.8(14)	91.9(14)	91.8(14)	91.6(15)	90.9(15)

In Figs. 4.8(a) and 4.8(b), the lattice constants a, b and c, and unit cell volume V are shown, respectively. The lattice constant b decreases, while a and c increase with increasing x. The crystal system goes from orthorhombic to quasi-cubic with increasing x. The unit cell volume shrinks as x increases and the decreasing rate grows at around $x = 0.2$. This change at $x = 0.2$ may be related with the magnetic transition.

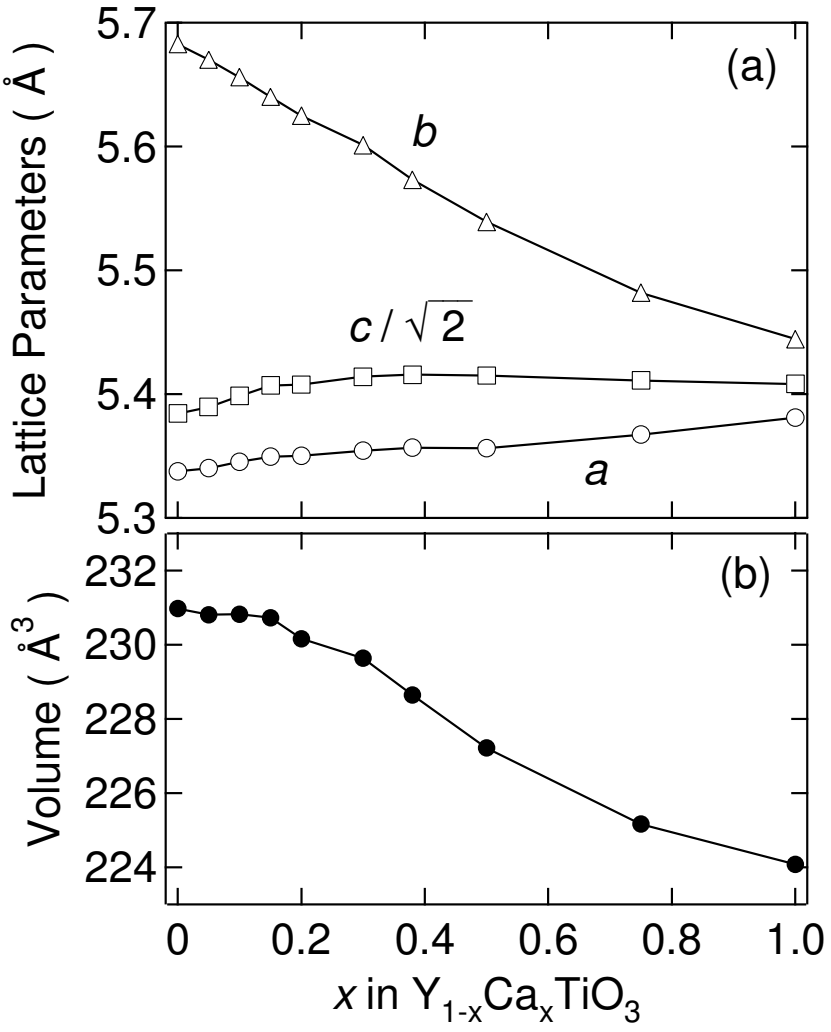

Figure 4.8: x dependences of (a) lattice constants and (b) volume in $Y_{1-x}Ca_xTiO_3$ at room temperature. Circles (◯), triangles (△) and squares (□) show lattice constants of a, b and $c/\sqrt{2}$ axes, respectively.

Figure 4.9 shows x dependence of the bond angles $\Theta_{\rm In}$ (angle in ab-plane) and $\Theta_{\rm Out}$ (angle along$c$-axis) which is related to the tilting of TiO_6. Both $\Theta_{\rm In}$ and $\Theta_{\rm Out}$ increase

linearly with increasing x. The tilting of TiO_6 relaxes from $\Theta_{\mathrm{In,Out}} \sim 140^\circ$ for $x = 0$ to $\sim 155^\circ$ for $x = 1$, though still distorted in a $GdFeO_3$-type.

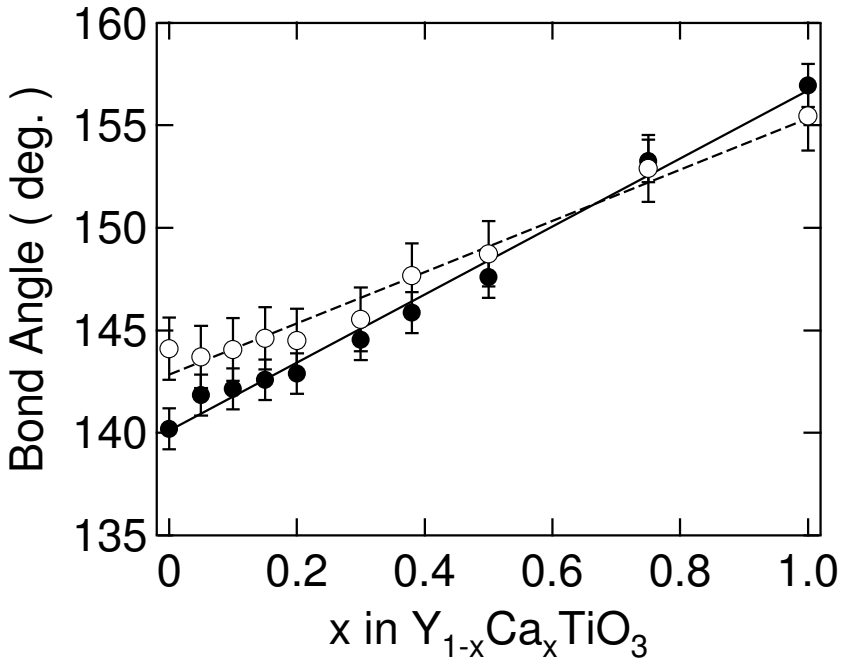

Figure 4.9: x dependences of the bond angle of Ti-O-Ti in $Y_{1-x}Ca_xTiO_3$ at room temperature. Open circles ($\circ$) and closed circles ($\bullet$) show the bond angle of Θ_{In} in-plane (ab-plane) and Θ_{Out} out-of-plane (along c axis), respectively.

Next, we focus differences in the Jahn-Teller (JT) distortion, *i.e.*, the Ti-O bond lengths and the O-Ti-O bond angles as shown in Figs. 4.10 and 4.11. The bond lengths Ti-O_x and Ti-O_z gradually decrease with increasing x. On the other hand, Ti-O_y slightly increases with increasing x up to 0.3 and decreases above $x = 0.3$. The ratio Δ^x_{JT} is close to unity in the highly doped region $0.4 \leq x \leq 1$, and Δ^y_{JT} is almost 1 in whole region $0 \leq x \leq 1$. Thus, it is found that TiO_6 octahedra which is alternately extended in ab-plane for $x = 0$ becomes almost regular above $x = 0.4$. This relaxation of JT distortion at $x = 0.4$ is consistent with the MI transition. In the insulating state, a TiO_6 octahedron is elongated in one direction and transfer t becomes anisotropic, then $3d$ electron at the Ti-site should be difficult to conduct. While, in the metallic region, TiO_6 octahedra regular and t is isotropic, then electron mobilizes easily. For the bond

angle between the coordinated axes, $\angle(xy)$ and $\angle(zx)$ are 90° in whole region $0 \leq x \leq 1$ as shown in Fig. 4.11(a). On the other hand, $\angle(yz)$ decreases from 93.5° at $x = 0$ to 92° at $x = 0.2$. Above $x = 0.2$, the bond angle of $\angle(yz)$ remains constant deviated from 90°. This means that the local crystal structure changes at $x_{\rm FP} = 0.2$, above which the ferromagnetism disappears. This change in $\angle(yz)$ is due to the y direction moving of oxygen O(2) as shown in Table. 4.3 and Fig. 4.11(b).

From these results, it is expected that $3d$ orbitals is splitted as shown in Fig. 4.12.

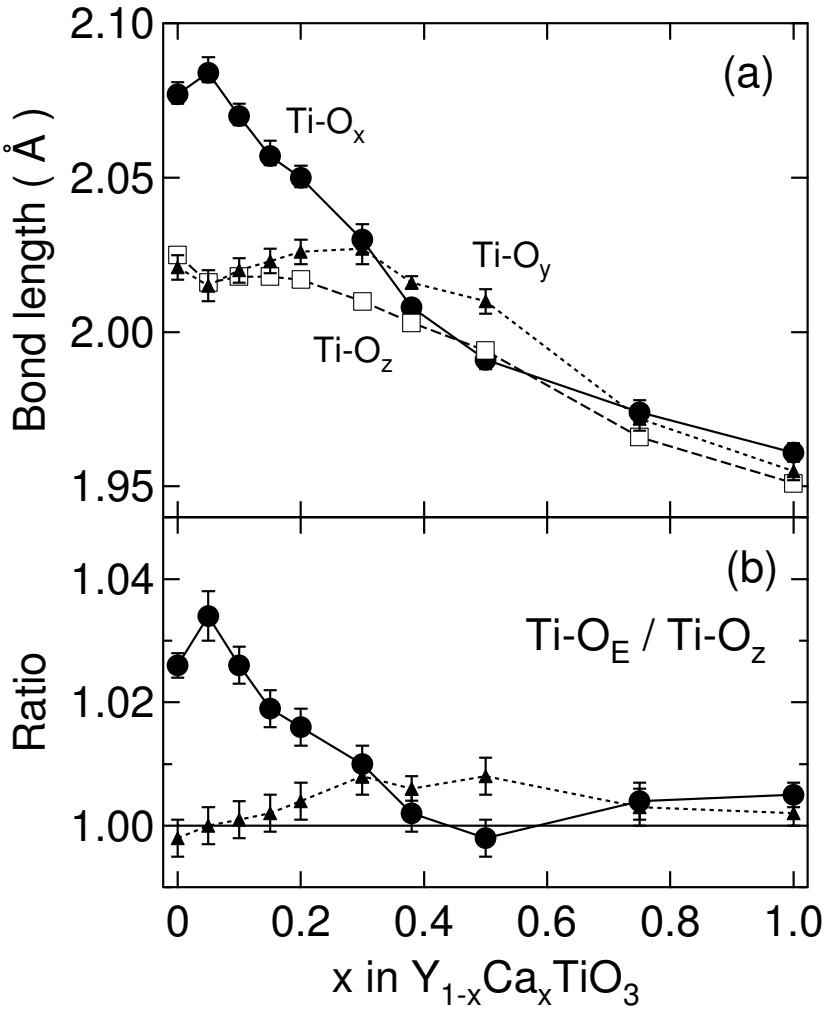

Figure 4.10: Ca dependences of (a) Ti-O bond lengths and (b) the ratio between Ti-$O_{\rm E}$ and Ti-O_z (E = x, y) in $Y_{1-x}Ca_xTiO_3$. Circles (•), triangles (▲) and open squares (□) show Ti-O bond lengths between Ti and O_x, O_y and O_z, respectively.

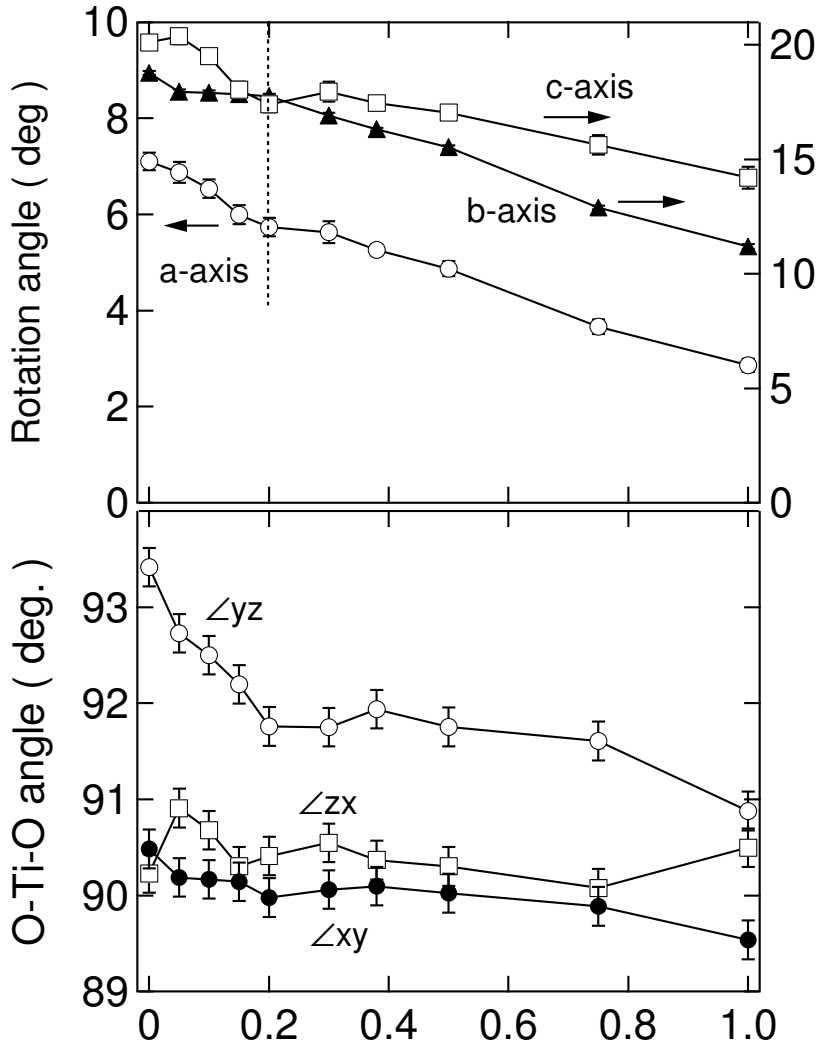

Figure 4.11: Ca dependences of (a) rotation angle around a-, b- and $c-$axis, and (b) O-Ti-O angle $\angle(xy)$, $\angle(yz)$ and $\angle(zx)$ in $Y_{1-x}Ca_xTiO_3$ at room temperature. Circles (◯), squares (□) and triangles (▲) in (a) show rotation angle around a-, b- and c-axis, respectively.

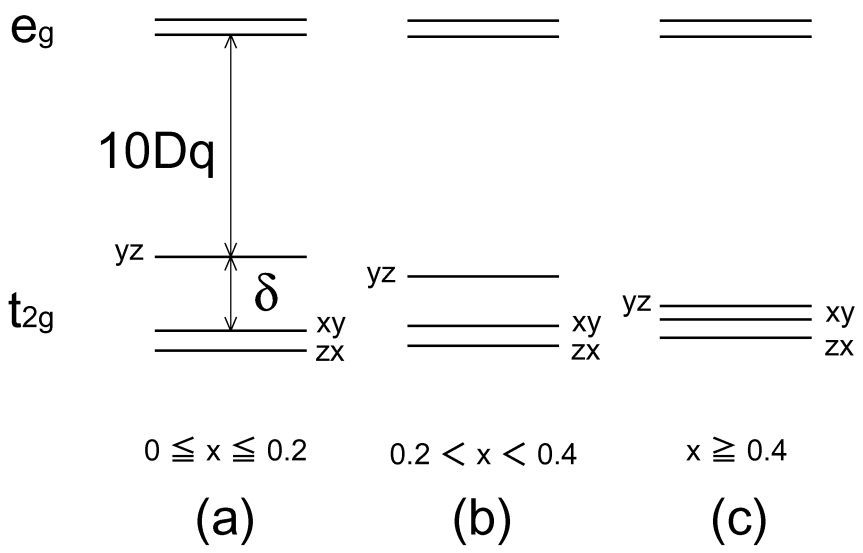

Figure 4.12: Schematic view of the energy level of the 3d orbitals (a) $0 \cdot x \cdot 0{:}2$, (b) $0{:}2 \cdot x \cdot 0{:}4$ and (c) $x \, , \, 0{:}4$ in $Y_{1\,i\,x}Ca_xTiO_3$.

4.4 Polarized neutron di®raction

The ¯nal analyzed results of the magnetic form factors ^1f are shown in Fig. 4.13 with open circles. The bars indicate the statistical uncertainties. Note that these magnetic re-°ections are \forbidden" ones in the usual magnetic structure factor calculation. It means that these magnetic re°ections should newly appear with the existence of the \antiferro" orbital ordering. These re°ections can be observed from the aspherical contribution of the spin density distribution. Therefore, we emphasize that the presence of the magnetic re°ections at these forbidden reciprocal points is a strong evidence for the existence of the antiferro orbital ordering in $Y_{1\,i\,x}Ca_xTiO_3$ ($x \cdot 0{:}15$).

Theoretical calculations by means of unrestricted Hartree-Fock approximation by Mizokawa and Fujimori predict orbital ordering in $YTiO_3$ as expressed by the following:

$$
\begin{aligned}
|a_1\rangle &= c_1|z_1x_1\rangle + c_2|x_1y_1\rangle \\
|a_2\rangle &= c_1|y_2z_2\rangle - c_2|x_2y_2\rangle \\
|a_3\rangle &= c_1|z_3x_3\rangle - c_2|x_3y_3\rangle \\
|a_4\rangle &= c_1|y_4z_4\rangle + c_2|x_4y_4\rangle;
\end{aligned}
$$

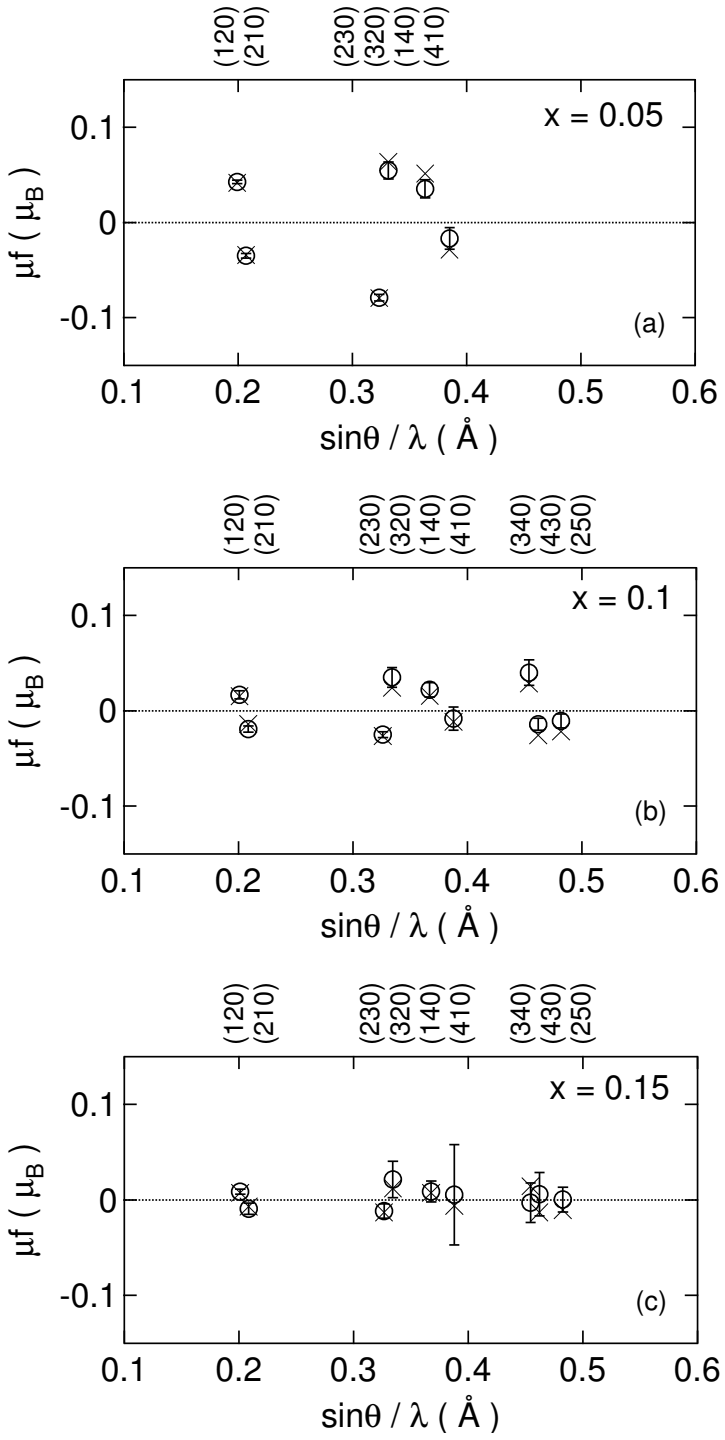

Figure 4.13: The magnetic form factors indicated by open circles (○) with error bars. The values calculated from the obtained wave functions are also plotted with crosses (×).

where $|z_n x_n\rangle$, $|y_n z_n\rangle$ and $|x_n y_n\rangle$ denote the wave function of irreducible representation in the t_{2g} [34] and c_1/c_2 denotes the ratio of the wave function with the normalization condition as $c_1^2+c_2^2 = 1-x$. Here, it is noted that the bond lengths TiO_x and Ti-O_y are the longest in the TiO_6 octahedron due to the JT distortion for each site $n = odd$ and $even$, respectively. In order to determine the coefficient c_1, we compared the experimental results with the theoretical model. In this case, the magnetic form factor $f_n(\boldsymbol{Q})$ theoretically calculated by Blume [57] and Trammel [58], with neglecting the orbital angular momentum term as a first-order approximation, can be expressed as,

$$\begin{aligned} f_n(\boldsymbol{Q}) &= \langle j_0 \rangle \\ &\quad -\frac{5}{14}\left[3\cos^2\theta_n - 1 + 3\sin^2\theta_n\left\{(c_2^2-c_1^2)\cos 2\phi_n + 2c_1c_2\sin 2\phi_n\right\}\right]\langle j_2\rangle \\ &\quad -\frac{3}{14}\left[35\cos^4\theta_n - 30\cos^2\theta_n + 3 - 5\cos^2\theta_n(7\cos^2\theta_n - 1)\right. \\ &\qquad \left.\times\left\{(c_2^2-c_1^2)\cos 2\phi_n + 2c_1c_2\sin 2\phi_n\right\}\right]\langle j_4\rangle, \end{aligned} \tag{4.1}$$

where θ_n and ϕ_n ($n = 1 \sim 4$) denote the spherical coordinates of the scattering vector $\boldsymbol{Q}$ relative to the quantization axes at site n and $\langle j_k\rangle$ ($k = 0$, 2 and 4) are expectation value of the spherical Bessel functions given in ref. [59]. We calculate $\mu_H f_n^{\rm calc}$ with c_1, c_2 and μ_H as unknown parameters by using eq. (4.1), and evaluate the goodness-of-fitting S as expressed the following:

$$S = \sqrt{\sum_j \frac{\left(\mu f^{\rm obs} - \mu_H f_j^{\rm calc}\right)^2}{w_j}},$$

where j is the number of the observed reciprocal points, w is the experimental statistics, $\mu f^{\rm obs}$ is the observed magnetic form factor and μ_H is the magnetic moment of $3d$ electrons.

In Fig. 4.14, we show the c_1 and μ_H variations of S classified by the shading with intervals of 2.5. In the pure white ares, S is moe than 30 and in the black one, S is less than 2.5. We determined the best-fitted parameters which give the smallest $S = 1.1$, 1.3 and 0.5 for $x = 0.05$, 0.1 and 0.15, respectively. The parameters which give the smallest S are listed in Table. 4.5.

The coefficient c_1^2 of $0.5 = (0.71)^2$ for $x = 0.05$ is almost the same value of $0.6 = (0.77)^2$ for $x = 0$. This means the orbital ordering is stable for small diluting Ti^{3+} with Ti^{4+}.

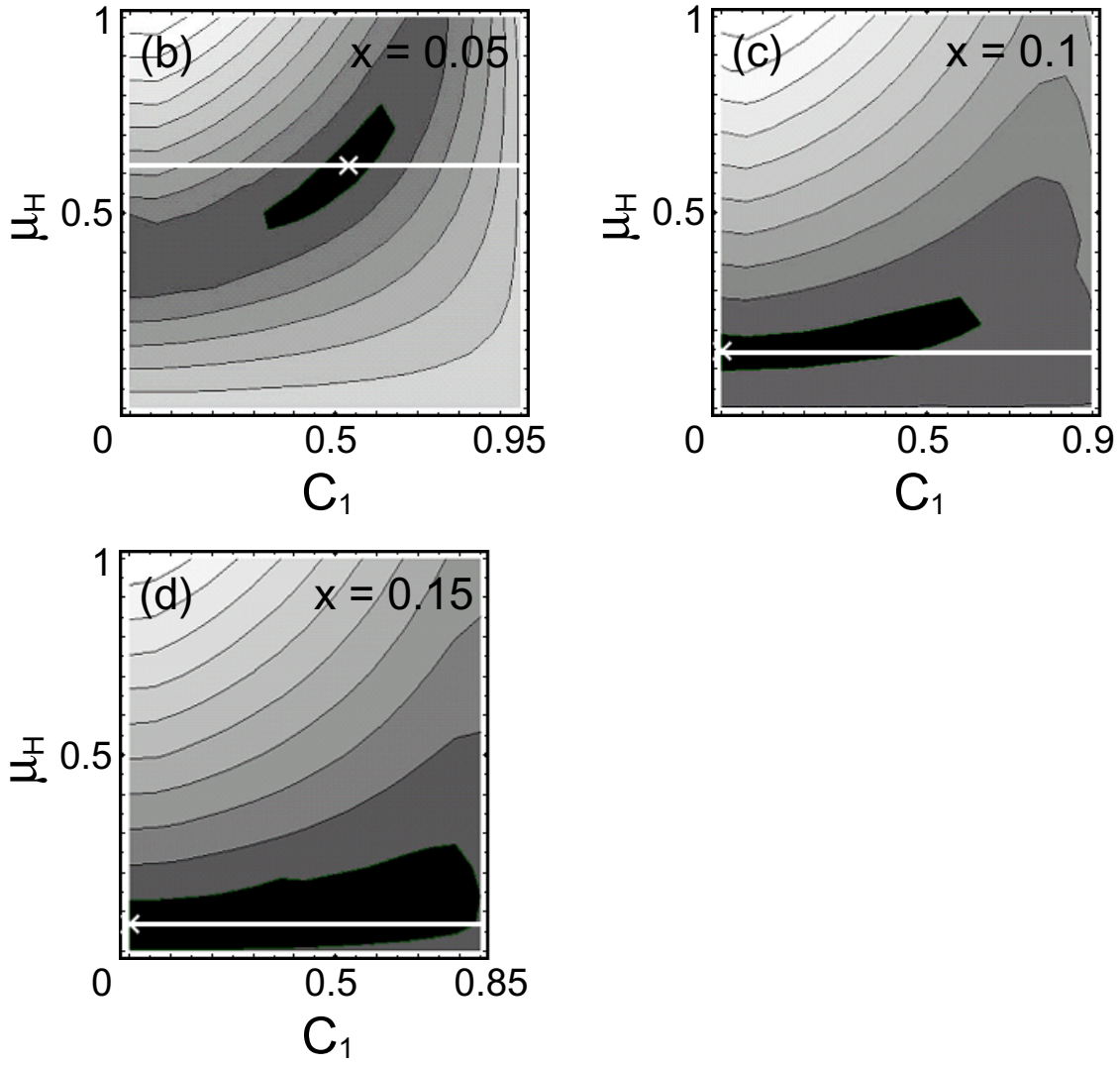

Figure 4.14: The c_1^2 and μ_H variations of the goodness-of-fitting S classified by the shading. S becomes smaller as the color of the area becomes more black. The white crosses denote the smallest S.

However, c_1^2 becomes 0 above $x = 0.1$ in analysis. But this value is uncertain due to the largeness of possible range of c_1^2 within the analytical error. Then, we could not determine the unique wave functions for $0.1 \leq x \leq x_{\mathrm{FP}}$. Anyway, it is found that the strong evidence of orbital ordering is obtained by the polarized neutron diffraction $x \geq x_{\mathrm{FP}}$. From these results, it is suggested that the dispersion of the ordered orbitals would increase toward the magnetic transition $x = x_{\mathrm{FP}}$.

Table 4.5: The fitting parameters c_1^2 and μ_H for comparison between the observed magnetic form factors and calculated ones in $Y_{1-x}Ca_xTiO_3$ ($x = 0.05$, 0.1 and 0.15). $\mu_{5\mathrm{T}}$ is estimated from the measurements of the magnetization at 2 K.

x	c_1^2	μ (μ_B)	
		μ_H	$\mu_{5\mathrm{T}}$
0.0	0.6	0.72	0.84
0.05	0.5	0.62	0.78
0.1	0	0.14	0.69
0.15	0	0.07	0.51

4.5 Resonant x-ray scattering

We have measured the absorption spectra of a titanium foil (50 μm thickness) near Ti K-absorption edge to calibrate the incident x-ray energy in every experiments. The absorption spectrum of the titanium foil has a small peak at the K-absorption edge as shown by an arrow in Fig 4.15. The actual energy value was 4.9665 keV in this case. We calibrated the observed energy by shift to the standard value of 4.9645 keV in ref. [60].

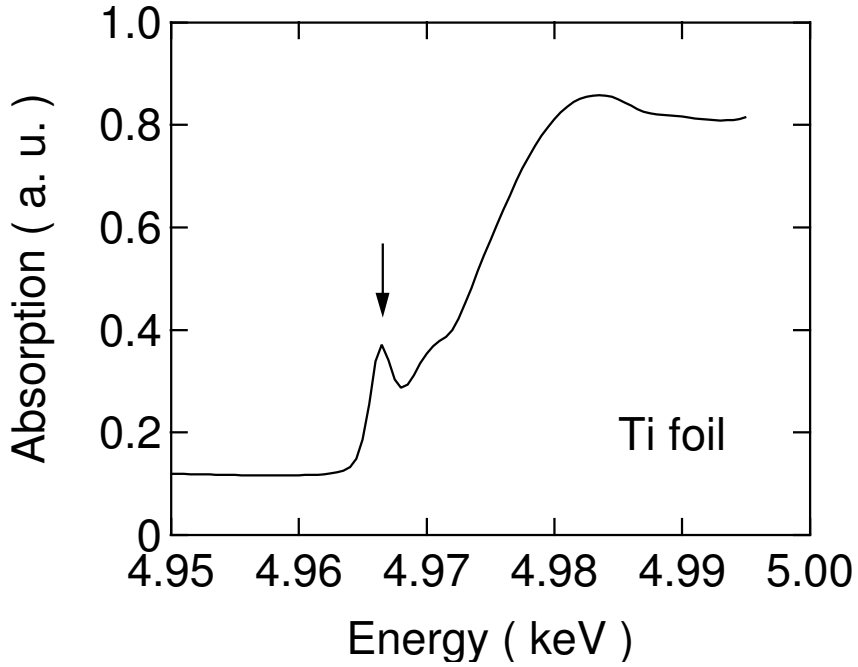

Figure 4.15: Absorption spectrum of Ti foil near a titanium K-absorption edge.

For the investigation of the orbitally ordered state of Ti $3d$-electron in $Y_{1-x}Ca_xTiO_3$ ($0 < x \leq 0.75$), we have studied the RXS at the "*forbidden*" reflections, (0 0 1), (0 1 1) and (1 0 0), near Ti K-edge. To avoid contaminations due to multiple scattering (MS), the energy dependence was measured at several azimuthal angles. The energy dependences of RXS intensity at (0 0 1), (0 1 1) and (1 0 0) free from the MS are shown in Fig 4.16 (a), (b) and (c), respectively. Figs. 4.17 (a), (b) and (c) show the magnified figure near pre-edge energy ($E \sim 4.972$ keV) at (0 0 1), (0 1 1) and (1 0 0), respectively. To correct variations dependent on sample shapes, the intensities of these forbidden reflections are normalized by the intensitied of the fundamental reflection peaks of (0 0 2), (0 2 2)

and (2 0 0), respectively. Furthermore, the normalized intensities are again normalized by the respective structure factors of the fundamental reflection peaks estimated from Rietveld analysis for Ca concentration dependence. The energy spectrum at the (0 0 1) shows three resonant peaks at 4.972 keV (pre-dege), 4.98 keV (main-dege) and 4.992 keV, and one shoulder at 4.989 keV. At the (0 1 1) reflection, four peaks are observed at 4.972 keV (pre-dege), 4.982 keV (main-edge), 4.986 keV and 4.993 keV. At the (1 0 0) reflection, six peaks are observed at 4.972 keV (pre-dege), 4.979 keV (main-edge), 4.982 keV, 4.993 keV, 5.001 keV and 5.008 keV. In each reflection, several resonant peaks are observed in $Y_{1-x}Ca_xTiO_3$ at the energy higher than the main-edge energy, although only one RXS peak was observed in manganite systems [18, 24]. The RXS energy spectrum of $Y_{1-x}C_xTiO_3$ are similar to the case of YVO_3 [21].

We discuss whether Ca the concentration dependences of the RXS intensities are the same or not for each peak. Fig. 4.18 shows the Ca concentration, x, dependences of the RXS at the (0 0 1). The x-dependences of the RXS are classified to two types as following: (1) pre-edge, and (2) main-edge and others at higher energies. The pre-dege intensity decreases rapidly with increasing x up to $x \sim 0.2 = x_{\rm FP}$ and vanishes at $x \sim 0.4 = x_{\rm MI}$. On the other hand, both the intensity at the main-edge energy and those at higher energies are almost constant with increasing x up to 0.1 and gradually decrease up to $x = 0.75$. Thus, x dependence of the RXS at pre-edge is different from that at main-edge. This fact means that the RXS at pre-edge originates from the mechanism different from that at main-edge. From these results, it is found that the RXS intensities depend on the excitation energy.

Second, we focus on the azimuthal angle Ψ dependences of the RXS intensities at pre-edge and main-edge. It is important that the intensity of the RXS depends on the difference of Ψ from the fundamental reflections. The Ψ dependence of the RXS intensities directly provides the information of the symmetry on the anisotropic structure factor. Figs. 4.19 (a), (b), (c) and (d) show the Ψ dependences of the RXS at (0 0 1), (1 0 0), (0 1 1) at $\sigma \rightarrow \pi'$ scattering and (0 1 1) at $\sigma \rightarrow \sigma'$ scattering for $x = 0.1$, respectively. The azimuthal angle Ψ is defined as follows; $\Psi = 0$ when $\sigma \parallel b$-axis of sample for (a) and (b), and $\Psi = 0$ when $\sigma \parallel a$-axis for (c) and (d). Ψ dependences of the (0 0 1) and

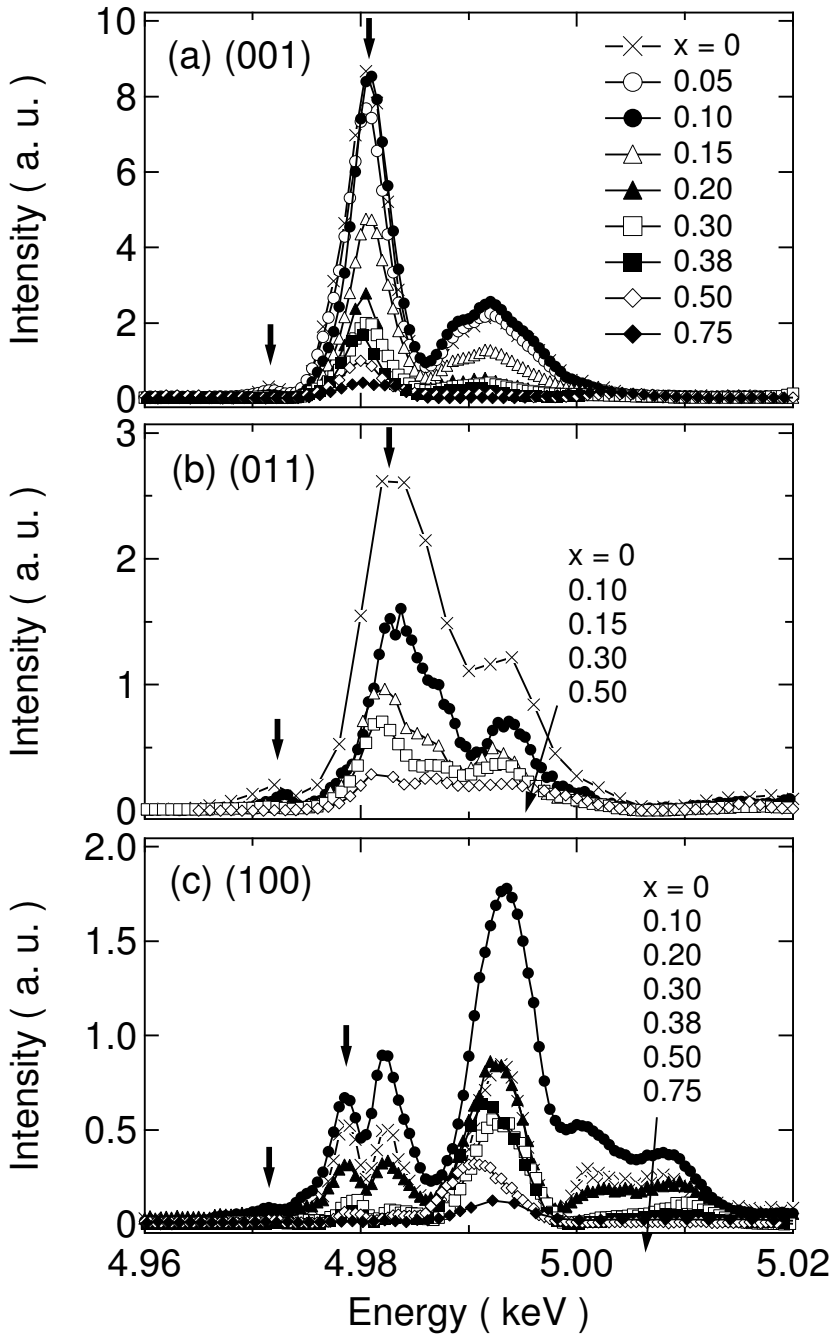

Figure 4.16: Energy dependences of RXS at (a) (0 0 1), (b) (0 1 1) and (c) (1 0 0) in $Y_{1-x}Ca_xTiO_3$.

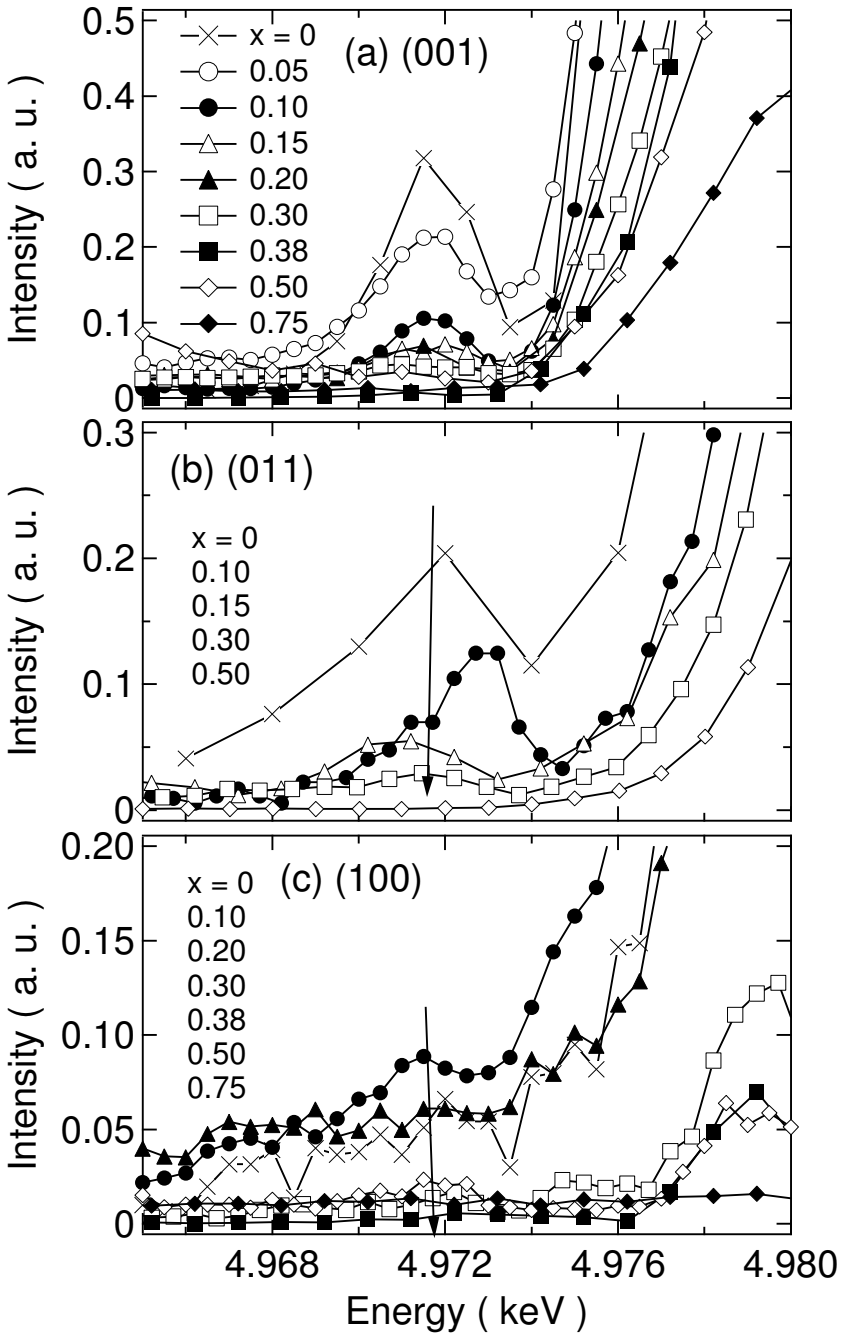

Figure 4.17: Energy dependences of RXS near $E \sim 4.972$ keV (pre-dege) at (a) (0 0 1), (b) (0 1 1) and (c) (1 0 0).

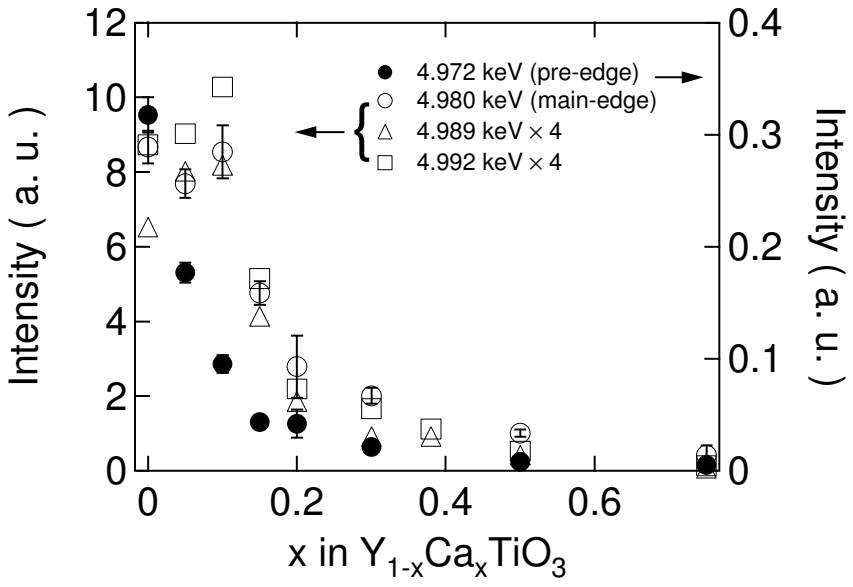

Figure 4.18: Ca concentration dependences of RXS at (0 0 1) reflection.

(1 0 0) reflections exhibit two-fold symmetries. At the (0 1 1) reflection, on the other hand, the Ψ dependence at $\sigma \rightarrow \pi'$ scattering has a period of 360° and that at $\sigma \rightarrow \sigma'$ scattering shows a four-fold symmetry as shown in Figs. 4.19 (c) and (d), respectively. For $0 < x \leq 0.5$, the Ψ dependences of the RXS coincide with those of $YTiO_3$ (see Fig. 2 in ref. [19]). The Ψ dependence at the pre-edge agree with those at the main-edge in $Y_{1-x}Ca_xTiO_3$. From these results, the RXS at the pre-edge by $1s \rightarrow 3d$ transition seems to arise from a $1s \rightarrow 4p$ dipole transition by induced the hybridization between the Ti $4p$ electrons and the neighboring Ti $3d$ electrons like the case of $YTiO_3$. Hence, the RXS intensity at the pre-edge can be considered as the order parameter of the orbital ordering.

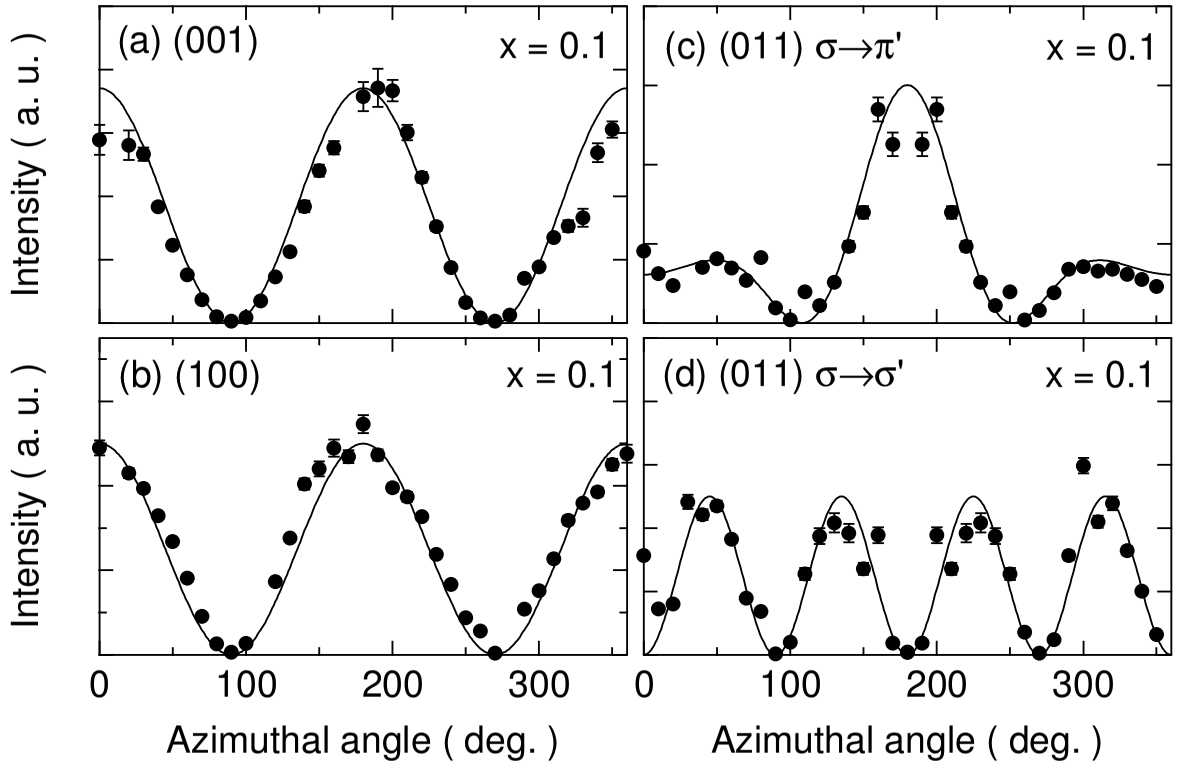

Figure 4.19: Energy dependences of RXS near $E \sim 4.972$ keV (pre-dege) at (a) (0 0 1), (b) (0 1 1) and (c) (1 0 0).

Then, we focus on the Ca concentration, x, dependences of the RXS at the pre-edge energy. Fig. 4.20 (a) shows the x dependences of the RXS at (0 0 1) and (0 1 1) reflections at the pre-edge energy in $Y_{1-x}Ca_xTiO_3$. Here, wo don't touch the RXS intensities at the (1 0 0) reflection at the pre-edge energy because we can not precisely estimate due to small signal-noise ratios in our experimental accuracy. Both RXS intensities at the (0 0 1) and (0 1 1) reflection at the pre-edge energy rapidly decrease with increasing x up to 0.15 $\sim$ 0.2 and vanish at $x = 0.4$. It means that the orbital ordering is strongly suppressed with increasing x up to $x_{\rm FP} = 0.2$, where magnetic order disappears, and vanishes at $x_{\rm MI} = 0.4$, where metallic phase is stabilized. x dependence of the bond angle $\angle(yz)$ between local coordination axes shows a tendency to decrease with increasing x up to $x_{\rm FP}$ and is become a constant value of 92° above $x_{\rm FP}$ as shown in Fig. 4.20 (b). For $x \geq x_{\rm MI}$, the ratio in bond lengths between Ti-O_x and Ti-O_z in TiO_6 becomes 1. Namely, the JT distortion is released and the TiO_6 octahedron becomes isotropic for $x \geq x_{\rm MI} = 0.4$. From these results, it is found that the orbital ordering becomes to be strongly suppressed with increasing x from 0 to $x_{\rm FP}$ and vanishes at $x_{\rm MI}$.

Next, we discuss the Ca concentration, x, dependences of the RXS at the main-edge energy. Fig. 4.21 shows the x dependences of the RXS at the (0 0 1), (0 1 1) and (1 0 0) reflections at the main-edge energy. The RXS intensities gradually decrease with increasing x up to 0.75 and the decreasing rate slows down above $x = 0.3$. In the metallic phase of $x \geq x_{\rm MI} = 0.4$, the RXS intensity becomes less than one-tenth of that for $x = 0$. This RXS intensity has small relation to the orbital ordering, because it is found that the orbitally ordered state is vanished above $x_{\rm MI}$ from the RXS intensities at pre-edge. The RXS intensity at the main-edge seems to be caused by the energy level splitting of the Ti $4p$ orbitals based on the theoretical model by Igarashi and there is three possible origins as following. The first is that the energy level splitting is arised from the JT distortion, the second is the tilts of the neighboring octahedron, and the last is that the Coulomb interaction between the Ti $3d$ and $4p$ orbitals. The first model is impossible because the JT distortion is released above $x_{\rm MI}$. In addition, this mechanism can not explain the Q-position dependence, the differences between three reciprocal lattice vectors, of the RXS intensity in $YTiO_3$ [19]. The second model is based on the deviation from 180° of the

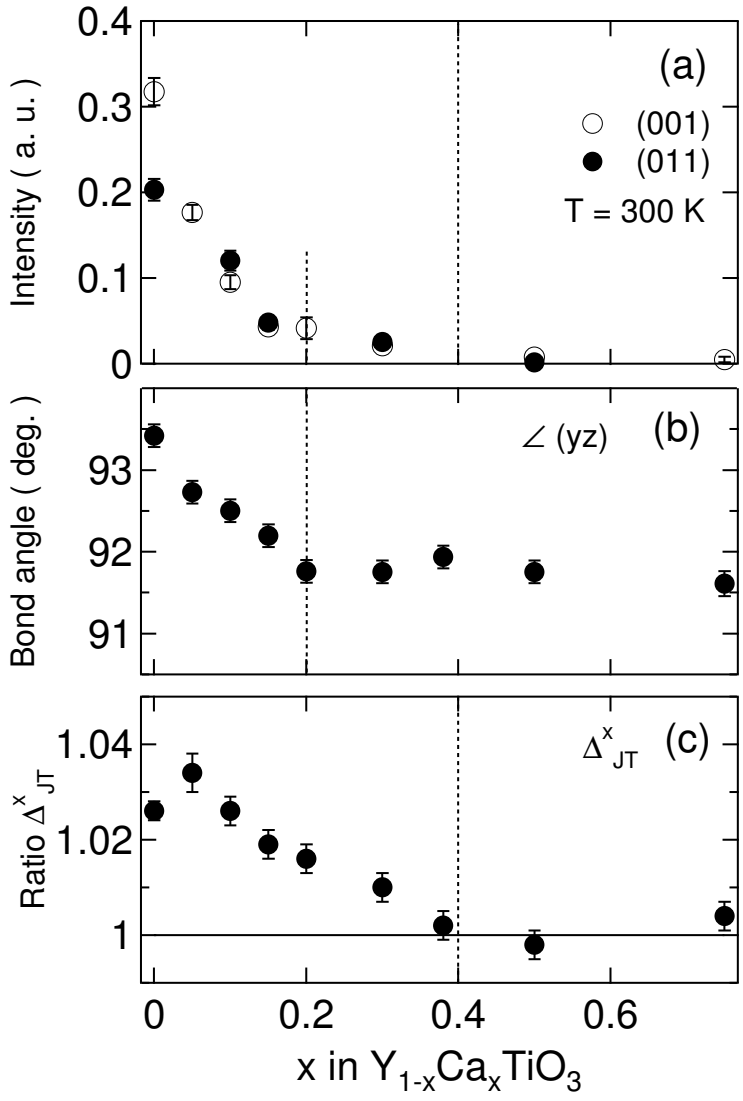

Figure 4.20: Ca concentration dependences of (a) the RXS at pre-edge ($E \sim 4.972$ keV), (b) bond angle between local coordination axes of O_y-Ti-O_z and (c) ratio $\Delta^x_{\rm JT}$ = Ti-O_x/Ti-O_z.

Ti-O-Ti tilting angle. These deviation does not change extremely; (140° for $x = 0$ and 147° for $x = 0.5$). Then, the RXS intensity originated from the tilting of the neighboring octahedron should be almost independent of x. We can not explain the difference of the RXS intensities ten times as large as between $x = 0$ and $x = 0.5$. As a result, the RXS intensity is expected to be originated from the third mechanism, coulomb interaction in Ti $3d$ and $4p$ orbitals.

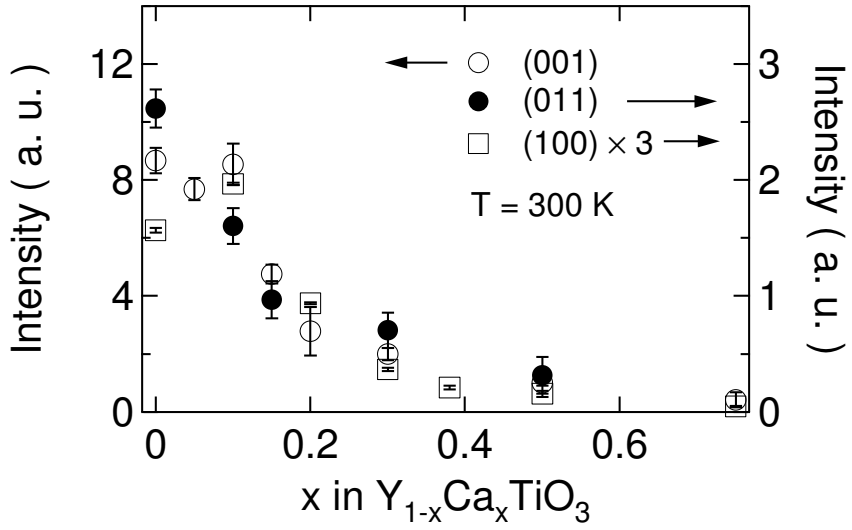

Figure 4.21: Energy dependences of RXS near $E \sim 4.972$ keV (pre-dege) at (0 0 1), (0 1 1) and (1 0 0) reflections.

At last, we describe about the wave functions of the orbital ordered state. From the ratios between three RXS reflections, we can estimate the coefficient c_1 by the model calculation based on the Coulomb mechanism [19]. As shown in Fig. 4.22 (a), these ratios does not change with increasing x, therefore, the coefficient c_1 should be same. In fact, the rotation angle r_x for $x = 0.5$, which is related to c_1, is determined to be the same value of 45±10° as that for $x = 0$. The atomic scattering factor tensor of the Ti ion was determined from measurements of the azimuthal angle, polarization. The anisotropic component of a tensor, Δf_a, was also determined as shown in Fig 4.22.

In conclusion,we have utilized the resonant x-ray scattering techniques to study systematically the orbital ordering of the Ti $3d$ orbitals in $Y_{1-x}Ca_xTiO_3$. It is found that the x dependence at the pre-edge ($E \sim 4.972$ keV) is different from that at the main-edge ($E \sim 4.982$ keV) as following. The RXS intensities at the pre-edge rapidly decrease with increasing x up to $x_{\rm FP}$ and vanish at $x_{\rm MI}$, but the RXS intensity at the main-edge energy has no such relation. We have also performed the powder x-ray diffraction to examine the orbitally ordering state through the JT distortion in the crystal structure. The orbital states derived from the anisotropy of the Ti-O bond length are consistent with that those from the RXS at the pre-edge. In the insulating phase of $Y_{1-x}Ca_xTiO_3$ ($x < 0.4$), we have succeeded to experimentally confirm the existence of the orbital ordering with the RXS at room temperature.

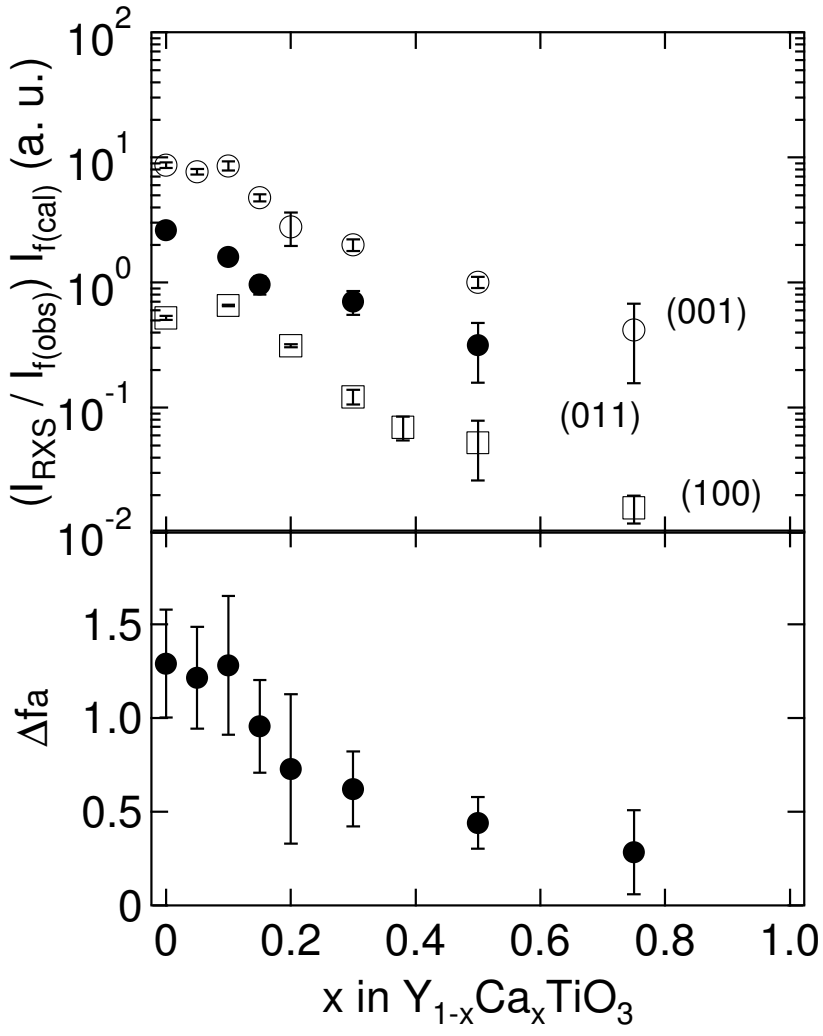

Figure 4.22: x dependences of (a) RXS intensities at main-edge and (b) Δf_a in $Y_{1-x}Ca_xTiO_3$. RXS intensities are normalized by observed and calculated fundamental peaks.

Chapter 5

Summary

In order to investigate the origin of the temperature-induced metal-insulator (MI) transition in $Y_{1-x}Ca_xTiO_3$ at $x \sim 0.39$ and clarify the role of the orbital degree of freedom in the magnetic transition and metal-insulator transition, three approaches have been taken in the present study: (1) a comparison between the Ca substitution effect and pressure effect on the MI transition, (2) Rietveld analysis of the crystal structure, *i.e.*, $GdFeO_3$-type distortion and Jahn-Teller distortion, (3) observation of orbital ordering by polarized neutron diffraction (PND) and resonant x-ray scattering (RXS) techniques.

(1) We compared the Ca substitution effect and pressure effect on the transport and the structural properties. We measured the electrical resistivity $\rho(T)$ for $0.37 \leq x \leq 0.41$ and powder x-ray diffraction (XRD) at ambient pressure. For $x = 0.37$ and 0.39, the MI transitions occur at $T_{\rm MI} = 100$ K and 150 K on cooling, respectively. Powder x-ray diffraction analysis showed that the monoclinic phase separates into the monoclinic phase and low-temperature orthorhombic (LTO) phase on cooling below $T_{\rm PS} = T_{\rm MI}$. This LTO phase is found to be a metallic phase from the fact that the residual resistivity decreases when the volume fraction of LTO increases. For $x = 0.37$, we measured $\rho(T)$ and XRD under pressure. The value of $T_{\rm MI}$ (100 K at $P = 0$ GPa) increases with increasing pressure, and eventually the metallic phase is stabilized even at room temperature under $P = 1.5$ GPa. The phase separation temperature agrees well with the MI transition temperature, and both temperatures increase linearly with increasing x or pressure. These results indicate that the MI

transition in $Y_{1-x}Ca_xTiO_3$ is not a simple Mott-Hubbard type but is caused by the percolation of the metallic LTO domains.

(2) Rietveld analysis of powder x-ray diffraction data at room temperature has been done for the samples in the whole range $0 \leq x \leq 1$. It is found that the tilting angle of the TiO_6 octahedron ($GdFeO_3$-type distortion; the bond angle of Ti-O-Ti which is related to the magnitude of superexchange interaction) increases monotonously with increasing x from 0 to 1. On the other hand, the angle between the local coordination y and z axes along the Ti-O bond directions decreases from 93.5° for $x = 0$ to 92° for $x = 0.2$. Above $x = 0.2$, two Ti-O bond lengths in the ab plane become almost equal, *i.e.*, Jahn-Teller distortion is released. This structural change should be resemble for the disappearance of the ferromagnetism at $x = x_{\rm FP}$.

(3) In the ferromagnetic region $x \leq 0.2$, we measured the magnetic form factors of Ti ions by means of PND in external fields parallel to the $c-$axis. The PND intensities have been observed at "*forbidden*" reflections in the conditions of $h + k = 2n + 1$, where h and k are the Miller indexes and n is integer. By comparing the observations with the model of orbital ordering configuration, we have determined the wave functions based on the model assuming $c_1|zx\rangle + c_2|xy\rangle$ $(c_1^2 + c_2^2 = 1)$ at site 1, for example. The coefficient c_1 is determined to be 0.77 for $x = 0$ and $x = 0.05$. Above $x = 0.1$, c_1 could not be determined uniquely due to the large range of analyzing error. It is suggested that the ferromagnetic order becomes unstable when the order of orbitals is weakened.

The RXS experiments were performed for $0 < x \leq 0.75$ at room temperature. The main-edge RXS intensity observed at the $1s \rightarrow 4p$ transition energy of $E = 4.982$ keV decreases linearly with increasing x up to 0.2, and more gradually decreases up to $x = 0.75$. On the other hand, the pre-edge intensity at the $1s \rightarrow 3d$ transition energy of $E = 4.972$ keV decreases rapidly with increasing x up to $x_{\rm FP}$ and vanishes at $x_{\rm MI}$. The x dependence of the RXS at the main-edge has no dramatic change at both $x_{\rm FP}$ and $x_{\rm MI}$ and is unlike any local lattice distortion. The x dependence of RXS at the pre-edge, on the other hand, is similar with that of Jahn-Teller (JT) distortion

of the TiO_6 octahedron. This means that the RXS intensity at the pre-edge reflects the orbitally ordered state. Thus, we have found that the ordering is weakened above $x = x_{\mathrm{FP}}$ but remains in the whole insulating phase for $x < x_{\mathrm{MI}}$.

By combining the above results (1), (2), and (3), it is found that the temperature-induced MI transition in $Y_{1-x}Ca_xTiO_3$ at $x \sim 0.39$ is not a simple Mott-Hubbard type but is result of percolation of the domains of the metallic low-temperature orthorhombic phase. For the insulating phase for $0 < x < 0.2$, the strong evidence of orbital ordering is obtained by both polarized neutron diffraction and resonant x-ray scattering experiments. The magnetic order becomes unstable when the order of orbitals is weakened, and the metallic phase appears when the order of orbitals melts for $x > 0.4$.

Acknowledgements

First I would like to express my sincere gratitude to my supervisor, Prof. Fumitoshi Iga. He took me as a student whereas I had worked as a system engineer for one year after graduation of my master course. Numerous valuable suggestions as well as helpful discussions have been provided by him as guidelines for my research.

I am also grateful to the laboratory group leader, Prof. Toshiro Takabatake for his helpful suggestions and valuable discussion.

They gave me a special chance to carry out various experiments at other institutes such as Photon Factory (KEK, Tsukuba), SPring-8 (JASRI, Hyogo), Hiroshima Synchrotron Radiation Center (Hi-SOR, Hiroshima University) and Neutron Scattering Laboratory of the University of Tokyo (JRR-3M, TOPAN, Tokai). I am grateful to Profs. Y. Murakami, H. Sawa, Drs. H. Nakao, N. Ikeda, H. Ohsumi, Y. Wakabayashi, M. Kubota, Mrs. S. Kodama and K. Kiyoto for the resonant x-ray scattering study. I am also grateful to Profs. M. Sakata, M. Takata, Drs. Y. Ohishi, E. Nishibori, K. Kato for the powder x-ray diffraction experiments and their analysis. I also express my hearty thanks to Prof. K. Shimada, Dr. M. Arita for x-ray photoemission experiments. I also thank Drs. H. Sawada, H. B. Huang, Profs. H. Namatame, M. Taniguchi, T. Jo, A. Kimura, Mrs. K. Yagi, M. Nagira for the linear dichroism study. I also thank Profs. J. Akimitsu and K. Hirota, Drs. T. Matsumura, K. Nakajima, Mrs. M. Saito and M. Togasaki for their support in the polarized neutron diffraction experiments.

I also thank Drs. T. Tsurui, N. Ogita, and Prof. M. Udagawa for Raman scattering study. I give my thanks to Prof. T. Suzuki, Mrs. H. Higaki and I. Ishii for the elastic property experiments.

I am very grateful to Dr. K. Umeo for his help in the electrical resistivity under

pressure and warmhearted encouragement. I wish to thank Drs. Y. Bando, J. Kitagawa, Y. Muro, D. Huo, E. Matsuoka, Y. Echizen and M. A. Avila for useful discussions. I express my thanks to Mrs. K. Kobori, T. Mukai, T. Nakano, S. Miyake, K. Uchihira, S. Kura, M. Takemura, and all other members in the laboratory during my student days.

Special thanks are given to Dr. Y. Shibata for the electron probe microanalysis and Prof. I. Nakamichi, and N. Yoshida, Y. Hanada for using liquid helium at the National Science Center for Basic Research and Development (N-BARD), Hiroshima University.

Finally, I thank my parents and my late grandparents for their endless love and giving me the talents to achieve this accomplishment, and my brother for rooting on my side.

Bibliography

[1] N. F. Mott: *Metal-Insulator Transitions, 2nd edition*, (Taylor & Francis, London, 1985).

[2] M. Imada, A. Fujimori and Y. Tokura: Rev. Mod. Phys. **70** (1998) 1039.

[3] Y. Taguchi, Y. Tokura, T. Arima and F. Inaba: Phys. Rev. B **48** (1993) 511.

[4] Y. Tokura, Y. Taguchi, Y. Moritomo, K. Kumagai, T. Suzuki and Y. Iye: Phys. Rev. B **48** (1993) 14063.

[5] Y. Taguchi, T. Okuda, M. Ohashi, C. Murayama, N. Môri, Y. Iye and Y. Tokura: Phys. Rev. B **59** (1999) 7917.

[6] S. A. Carter, T. F. Rosenbaum, J. M. Honig and J. Spalek: Phys. Rev. Let. **67** (1991) 3440.

[7] J. Zaanen, G. A. Sawatzky, and J. W. Allen: Phys. Rev. Lett. **55** (1985) 418.

[8] M. Itoh, M. Tsuchiya, H. Tanaka and K. Motoya: J. Phys. Soc. Jpn. **68** (1999) 2783.

[9] H. Kuwahara, Y. Tomioka, Y. Morimoto, A. Asamitsu, M. Kasai, and Y. Tokura: Science **270** (1995) 961.

[10] E. Nishibori, M. Takata, K. Kato, M. Sakata, Y. Kubota, S. Aoyagi, Y. Kuroiwa, M. Yamakata and N. Ikeda: J. Phys. Chem. Solids **62** (2001) 2095.

[11] A. Fujiwara, K. Ishii, T. Watanuki, H. Suematsu, H. Nakao, K. Ohwada, Y. Fujii, Y. Murakami, T. Mori, H. Kawada, T. Kikegawa, O. Shimomura, T. Matsubara, H. Hanabusa, S. Daicho, S. Kitamura and C. Katayama: J. Appl. Cryst. **33** (2000) 1241.

[12] F. Izumi and T. Ikeda: Mater. Sci. Forum. **321-324** (2000) 198.

[13] H. Ichikawa, J. Akimitsu, M. Nishi and K. Kakurai: Physica B **281&282** (2000) 482.

[14] Y. Itoh and J. Akimitsu: J. Phys. Soc. Jpn. **40** (1976) 1333.

[15] J. Akimitsu, H. Ichikawa, N. Eguchi, T. Miyano, M. Nishi and K. Kakurai: J. Phys. Soc. Jpn. **70** (2001) 3475.

[16] M. Fabrizio, M. Altarelli, M. Benfatto: Phys. Rev. Let. **80** (1998) 3400.

[17] J. R. Hester, K. Tomimoto, H. Noma, F. P. Okamura, J. Akimitsu: Acta Crystallogr. B **53** (1997) 739.

[18] Y. Murakami, J. P. Hill, D. Gibbs, M. Blume, I. Koyama, M. Tanaka, H. Kawata, T. Arima, Y. Tokura, K. Hirota and Y. Endoh: Phys. Rev. Let. **81** (1998) 582.

[19] H. Nakao, Y. Wakabayashi, T. Kiyama, Y. Murakami, M. v. Zimmermann, J. P. Hill, D. Gibbs, S. Ishihara, Y. Taguchi and Y. Tokura: Phys. Rev. B **66** (2002) 184419.

[20] B. Keimer, D. Casa, A. Ivanov, J. W. Lynn, M. v. Zimmermann, J. P. Hill, D. Gibbs, Y. Taguchi and Y. Tokura: Phys. Rev. Lett. **85** (2000) 3946.

[21] M. Noguchi, A. Nakazawa, S. Oka, T. Arima, Y. Wakabayashi, H. Nakao and Y. Murakami: Phys. Rev. B **62** (2000) R9271.

[22] L. Paolosini, C. Vettier, F. de Bergevin, F. Yakhou, D. Mannix, A. Stunault, W. Neubeck, M. Altarelli, M. Fabrizio, P. A. Metcalf and J. M. Honig: Phys. Rev. Lett. **82** (1999) 4719.

[23] H. Nakao, K. Ohwada, N. Takesue, Y. Fujii, M. Isobe, Y. Ueda, M. v. Zimmermann, J. P. Hill, D. Gibbs, J. C. Woicik, I. Koyama and Y. Murakami: Phys. Rev. Lett. **85** (2000) 4349.

[24] Y. Murakami, J. P. Hill, D. Gibbs, M. Blume, I. Koyama, M. Tanaka, H. Kawata, T. Arima, Y. Tokura, K. Hirota and Y. Endoh: Phys. Rev. Lett. **81** (1998) 582.

[25] Y. Endoh, K. Hirota, S. Ishihara, S. Okamoto, Y. Murakami, A. Nishizawa, T. Fukuda, H. Kimura, H. Nojiri, K. Kaneko and S. Maekawa: Phys. Rev. Lett. **82** (1999) 4328.

[26] M. v. Zimmermann, J. P. Hill, D. Gibbs, M. Blume, D. Casa, B. Keimer, Y. Murakami, Y. Tomioka and Y. Tokura: Phys. Rev. Lett. **83** (1999) 4872.

[27] K. Nakamura, T. Arima, A. Nakazawa, Y. Wakabayashi and Y. Murakami: Phys. Rev. B **60** (2000) 2425.

[28] Y. Wakabayashi, Y. Murakami, I. Koyama, T. Kimura, Y. Tokura, Y. Moritomo, K. Hirota and Y. Endoh: J. Phys, Soc. Jpn. **69** (2001) 2731.

[29] J. García, G. Subías, M. G. Proietti, H. Renevier, Y. Joly, J. L. Hodeau, J. Blasco, M. C. Sánchez, and J. F. Bérar Phys. Rev. Lett. **85** (2000) 578.

[30] L. Paolasini, R. Caciuffo, A. Sollier, P. Ghigna, and M. Altarelli: Phys. Rev. Lett. **88** (2002) 106403.

[31] K. Hirota, N. Oumi, T. Mateumura, H. Nakao, Y. Wakabayashi, Y. Murakami and Y. Endoh: Phys. Rev. Lett. **84** (2000) 2706.

[32] H. Nakao, K. Magishi, Y. Wakabayashi, Y. Murakami, K. Koyama, K. Hirota, Y. Endoh and S. Kuni: J. Phys. Soc. Jpn. **70** (2001) 1857.

[33] D. F. McMorrow, K. A. McEwen, U. Steigenberger, H. M. Ronnow and F. Yakhou: Phys. Rev. Lett. **87** (2001) 057201.

[34] T. Mizokawa, D. I. Khomskii and G. A. Sawatzky: Phys. Rev. B **60** (1999) 7309.

[35] J. E. Greedan: J. Less-Common Met. **111** (1985) 335.

[36] J. D. Garrett, J. E. Greedan and D. A. MacLean: Mat. Res. Bull. **16** (1981) 145.

[37] J. P. Goral, J. E. Greedan and Maclean: J. Solid State Chem. **43** (1982) 244.

[38] M. Tsubota, F. Iga, T. Takabatake, N. Kikugawa, T. Suzuki, I. Oguro, H. Kawanaka and H. Bando: Physica B **281&282** (2000) 622.

[39] K. Kumagai, T. Suzuki, Y. Taguchi, Y. Okada, Y. Fujishima and Y. Tokura: Phys. Rev. B **48** (1993) 7636.

[40] F. Iga, T. Nishiguchi and Y. Nishihara: Physica B **206&207** (1995) 859.

[41] F. Iga, Y. Nishihara, J. Sakurai and M. Ishikawa: Physica B **237&238** (1997) 14.

[42] F. Iga, N. Shirakawa, K. Murata, Y. Nishihara, T. Ishii, G. Oomi and Y. Uwatoko: Bull. Electrotech. Lab. **59** (1995) 459.

[43] F. Iga, T. Naka, T. Matsumoto, N. Shirakawa, K. Murata and Y. Nishihara: Physica B **223&224** (1996) 526.

[44] F. Iga, H. Fukuchi, I. H. Inoue and Y. Nishihara: *Proc. 9th Int. Conf. Ternary and Multinary Compounds, Yokohama, 1993,* Jpn. J. Appl. Phys. **32** (1993) Suppl. 32-3, p.332.

[45] K. Kato, E. Nishibori, M. Takata, M. Sakata, T. Nakano, K. Uchihira, M. Tsubota, F. Iga and T. Takabatake: J. Phys. Soc. Jpn. **71** (2002) 2082.

[46] E. S. Itskevich: CRYOGENICS. (1964) 365.

[47] T. Naka, T. Matsumoto, A. Matsushita, F. Iga, Y. Nishihara: Physica B **304** (2001) 27.

[48] T. Naka, T. Matsumoto, F. Iga and Y. Nishihara: Rev. High Pressure Sci. Technol. **7** (1998) 608.

[49] H. -D. Jostarndt, U. Walter, J. Harnischmacher, J. Kalenborn, A. Severing and E. Holland-Moritz: Phys. Rev. B **46** (1992) 14872.

[50] J. Burgy and E. Dagotto and M. Mayr: Phys. Rev. B **67** (2003) 014410.

[51] M. Mayr, A. Moreo, J. A. Vergés, J. Arispe, A. Feguin and E. Dagotto: Phys. Rev. Let. **86** (2001) 135.

[52] K. Yoshida: Phys. Rev. B **60** (1999) 9325.

[53] A. Urushibara, Y. Moritomo, T. Arima, A. Asamitsu, G. Kido and Y. Tokura: Phys. Rev. B. **51** (1995) 14103.

[54] Y. Moritomo, A. Asamitsu and Y. Tokura: Phys. Rev. B. **51** (1995) 16491.

[55] D. A. Crandles, T. Timusk and J. E. Greedan: Phys. Rev. B. **44** (1991) 13250.

[56] B. Keimer, D. Casa, A. Ivanov, J. W. Lynn, M. v. Zimmermann, J. P. Hill, D. Gibbs, Y. Taguchi and Y. Tokura: Phys. Rev. Lett. **85** (2000) 3946.

[57] R. E. Watoson, and A. J. Freeman: Acta Crystallogr. **14** (1961) 27.

[58] G. T. Trammel: Phys. Reb. **92** (1953) 1387.

[59] R. E. Watoson, and A. J. Freeman: Acta Crystallogr. **14** (1961) 27.

[60] J. A. Bearden: Rev. Mod. Phys. **39** (1967) 78.